Influence of Joint Conformity on the Failure Mechanisms of the Glenoid Implant – a finite element analysis

Maria do Carmo Rocha e Melo Belard Raimundo

Thesis to obtain the Master of Science Degree in

Biomedical Engineering

Supervisor(s): Prof. João Orlando Marques Gameiro Folgado

Prof. Carlos Miguel Fernandes Quental

Examination Committee

Chairperson: Prof. Fernando Manuel Fernandes Simões

Supervisor: Prof. João Orlando Marques Gameiro Folgado

Members of the Committee: Dr. André Paulo Galvão de Castro

October 2021

Declaration

I declare that this document is an original work of my own authorship and that it fulfills all the requirements of the Code of Conduct and Good Practices of the Universidade de Lisboa.

Abstract

Glenoid loosening is the most common complication after anatomic total shoulder arthroplasty, making up 80% of long term complications. Several mechanisms lead to glenoid loosening, including the failure of the implant itself (wear or fracture), lack of support of the underlying bone and inadequate fixation. The glenoid implant has suffered many alterations in composition and design over the years and their influence on joint and implant stability has been studied. However, the understanding of the influence of articular conformity in glenoid loosening is still limited. This study aimed to understand whether the conformity of the joint influences the failure of the glenoid component. Therefore, finite element analyses of three articular configurations of 1mm, 3mm and 5mm radial mismatch, were performed. The joint reaction forces obtained using a multibody model of the upper limb for abduction and flexion movements in different degrees of motion were applied in the FE model. To assess the influence of joint conformity in the mechanisms of glenoid loosening three analyses were performed. Firstly, the humeral translations retrieved from the multibody model were analyzed for the different configurations. Secondly, the evaluation of the Von Mises stresses on the cement allowed for the analysis of the mechanical failure of the material under cyclic loading. Finally, to analyze the bone-cement interface, the Hoffman failure criteria was applied, using both normal and shear stresses on the interface. The results showed that the more conforming configuration has lower risks of failure under healthy physiological conditions when compared to less conforming designs.

Keywords: Anatomic total shoulder arthroplasty, Glenoid loosening, Failure mechanisms, Finite element analysis.

Resumo

A falha do componente da glenoide é a complicação mais comum da artroplastia total anatómica do ombro, correspondendo a 80% das complicações a longo prazo. Os mecanismos de falha da glenoide, incluem a falha do próprio implante (fratura ou desgaste), falta de suporte do osso e fixação deficiente. Este componente sofreu várias alterações ao longo dos anos a nível dos materiais e do design, cuja influência na estabilidade da prótese tem vindo a ser estudada. No entanto, o conhecimento da influência da conformidade articular nos mecanismos de falha é ainda reduzido. O objetivo deste estudo foi compreender a interferência da diferença radial na falha do implante. Assim, utilizou-se o método de elementos finitos para simular a artroplastia total do ombro para três diferenças radiais de 1mm, 3mm e 5mm. O modelo computacional do ombro foi sujeito a seis casos de força obtidos através de um modelo multicorpo do membro superior para os movimentos de abdução e de flexão. Para avaliar a influência da conformidade articular nos mecanismos de falha recorreu-se a três métodos. Primeiramente, avaliou-se as translações umerais obtidas pelo modelo musculosquelético para todas as configurações. Em segundo lugar, para avaliar a falha do cimento analisaram-se as respetivas tensões de von Mises. Finalmente, a interface osso-cimento foi avaliada através do critério de falha de Hoffman, recorrendo às tensões normais e de corte na interface. Os resultados mostraram que para uma maior conformidade articular o risco de falha da glenoide sobre condições fisiológicas e saudáveis é inferior do que para configurações com maior diferença radial.

Palavras-chave: Artroplastia anatómica do ombro, Falha da glenoide, Mecanismos de falha, Análise de elementos finitos.

Table of Contents

Declaration ..... *i*

Abstract ..... *iii*

Resumo ..... *v*

List of Figures ..... *ix*

List of Tables ..... *xiii*

List of Acronyms ..... *xv*

Chapter 1 ..... *1*

Introduction **1**

1.1 Motivation and Objectives 1

1.2 Outline of the Thesis 2

Chapter 2 ..... *5*

Concepts and considerations on Total Shoulder Arthroplasty **5**

2.1 Shoulder joint 5

2.2 Total Shoulder Arthroplasty 9

2.2.1 Anatomic TSA 10

2.2.2 Surgical Technique 13

2.2.3 Complications 18

2.2.4 State of the Art 21

2.3 Contributions of this thesis 23

Chapter 3 ..... *25*

Materials and Methods **25**

3.1 Geometric modeling of TSA 26

3.1.1 Glenohumeral joint 26

3.1.2 Implant Model 27

3.1.3 TSA complete model 30

3.2 Multibody modeling of TSA 31

3.3 Finite element modeling of TSA 33

3.3.1 Material properties 33

3.3.2 Mesh 34
3.3.3 Contact and interaction properties 36
3.3.4 Loading conditions 36
3.3.5 Boundary Conditions 37
3.4 Analysis of FE results 38
3.4.1 Evaluation of the cement stresses 38
3.4.2 Hoffman Criterion 38
Chapter 4 41
Results 41
4.1 GH joint translations after TSA 41
4.2 Finite Element Analysis 44
4.3 Analysis of the cement mantle stresses 45
4.4 Hoffman failure criterion 48
Chapter 5 51
Discussion 51
Chapter 6 55
Conclusions and future work 55
6.1 Conclusions 55
6.2 Future work 56
References 57
Appendix A 63

List of Figures

Figure 2.1: Joints of the shoulder girdle [9]. 6

Figure 2.2: Anterior (a) and posterior (b) view of the right scapula [10]. 6

Figure 2.3: Anterior and posterior view of the humerus [12]. 7

Figure 2.4: Anterior (a) and lateral (b) view of the ligaments and tendons of the glenohumeral joint [10]. 8

Figure 2.5: The rotator cuff muscles - subscapularis, supraspinatus, teres minor and infraspinatus [9]. 9

Figure 2.6:Total shoulder replacements: (a) reverse total shoulder arthroplasty and (b) anatomic total shoulder arthroplasty [13]. 10

Figure 2.7: Types of humeral components used in TSA: (a) Standard-length stem implant – DePuy Global® AP® System [16]; (b) Short-stem implant – Tornier AEQUALIS ASCEND™ FLEX Convertible Shoudler Arthroplasty System [17]; and (c) Stemless implant – Tornier SIMPLICITI™ Shoulder system [18]. 11

Figure 2.8: Design of different glenoid components: (a) keeled and (b) pegged all-polyethylene AEQUALIS™ PERFORM Anatomic Glenoid System ™ [22]; and (c) Metal-backed SMR Anatomic by Lima Corporate (adapted from [23]) 12

Figure 2.9: Surgical steps to perform the humeral head resection. (a) Use of the flat head gauge to assess the diameter and height of the head; (b) assembly of the head sizer followed by (c) placing of the center pin and (d) resection of the humeral head [16]. 14

Figure 2.10: (a) Humeral canal preparation, (b) Broach/trial stem insertion [16]. 15

Figure 2.11: Glenoid preparation for implantation. (a) Sizer disk and guide pin for center identification; (b) glenoid reaming using spherical reamer inserted into the guide pin [25]. 16

Figure 2.12: Glenoid trial to confirm the fit between the implant and the bone [16]. 16

Figure 2.13: (a) Peripheral peg drilling; (b) recommended order of peripheral peg hole preparation: 1) anterior-inferior 2) anterior- posterior 3) superior [26]. 17

Figure 2.14: Anchor peg system: (a) Central anchor peg covered with morselized bone paste [16] and (b) tissue integration surrounding the central anchor peg in vivo [27]. 17

Figure 2.15: Cement placement on the drilled peripheral holes (on the left) and final glenoid implantation (on the right) [28]. 18

Figure 2.16: Glenohumeral mismatch of 3mm [16]. 18

Figure 2.17: (A) Early postoperative x-ray of the shoulder. (B) 5-year postoperative x-ray of the GH joint with lucency around the all-polyethylene implant [36] 19

Figure 2.18: Rocking-horse phenomenon described by Franklin et. al. [3] as a result of eccentric loading and humeral head translation on the glenoid [42]. 20

Figure 3.1: Methodology used to study the failure mechanisms of the glenoid component after anatomic TSA. 25

Figure 3.2: Glenohumeral joint model provided by the research group .[60] 26

Figure 3.3: Sagittal (a) and frontal (b) view of the glenoid implant designed. 27

Figure 3.4: Scapula after glenoid reaming for bone preparation. 28

Figure 3.5: (a) Cement mantle for glenoid fixation and (b) glenoid-bone fixation. 29

Figure 3.6: Glenoid component implanted in the scapula. 29

Figure 3.7: Humeral components for simulation of TSA with different mismatches. From left to right: 26mm radius, 24mm radius and 22 mm radius. 30

Figure 3.8: (a) Humeral head cutting guide [16]; (b) cut humerus for implantation and (c) implanted humeral head. 30

Figure 3.9: Final TSA model for 3mm radial mismatch. 31

Figure 3.10: GH configurations for three TSA. (a) 5mm radial mismatch; (b) 3mm radial mismatch and (c) 1mm radial mismatch. 31

Figure 3.11: Muscoskeletal model used for defining loading conditions and analyzing GH translations [60]. 32

Figure 3.12: Bone density mapping for the scapula (middle) and the cut view of the scapula (right) and scale (left). 34

Figure 3.13: Mesh of the cement (a) and the glenoid (b). 34

Figure 3.14: Element size assignment for the scapula mesh (a) and final scapula mesh (b). 35

Figure 3.15: Reference point for load application on the humeral head center. 36

Figure 3.16: Rhomboid insertion in the scapula [9] and respective boundary condition. 37

Figure 4.1:Glenohumeral reaction forces during (a) abduction and (b) flexion for radial mismatches of 1mm, 3mm and 5mm. 42

Figure 4.2:Humeral translations over the glenoid during (a) abduction and (b) flexion. Positive ant-post translations correspond to anteriorly directed translations. Positive inf-sup translations correspond to superiorly directed translations. The markers on the lines correspond to the translations on specific frames of abduction and flexion, including, 14º, 30º, 50º, 70º, 90º and 110º of humeral elevation. 43

Figure 4.3: Contact pressures on the glenoid surface during abduction: (a) 30º of abduction; (b) 70º of abduction and (c) 110º of abduction. The color scale presented is applicable to all figures. 44

Figure 4.4: Von Mises stress distributions on the surface of the cement mantle for the three mismatches and the three load cases during abduction: (a) 30º abduction; (b) 70º abduction; (c) 110º abduction. The color scale presented is applicable to all figures. 46

Figure 4.5: Von Mises stress distributions on the surface of the cement mantle for the three mismatches and the three load cases during flexion: (a) 30º flexion; (b) 80º flexion; (c) 105º flexion. The color scale presented is applicable to all figures. 47

Figure 4.6: Cumulative percentage of nodes that are under a specific Von Mises stress or higher. 48

Figure 4.7: Hoffman number distributions for (a) 1mm mismatch; (b) 3mm mismatch and (c) 5mm mismatch. The orientation of the images is depicted in (a). The color scale presented is applicable to all figures. 49

Figure 4.8: Cumulative percentage of nodes with Hoffman number between 0 and 1. 50

Figure A.0.1: Contact pressure for all GH configurations for (a) 30º of flexion, (a) 80º of flexion and (c) 105º of flexion. The color scale presented is applicable to all figures. 63

List of Tables

Table 3.1: Software used to develop the FE models used to study the failure mechanisms of the glenoid component after anatomic TSA. 26

Table 3.2: Glenoid dimensions used in implant design [61]. 27

Table 3.3: Material properties for the glenoid implant and the bone cement [53]. 33

Table 3.4: Mesh summary for all components. 35

Table 3.5: Magnitude and direction of the load cases used in this analysis. 37

List of Acronyms

TSA	Total shoulder arthroplasty
GHOA	Glenohumeral Osteoarthritis
PE	Polyethylene
MBG	Metal-backed glenoid
FE	Finite element
FEM	Finite element model
PMMA	Polymethyl-metacrylate
UHMWPE	Ultra-high-molecular-weight polyethyllene
CT	Computed tomography

Chapter 1

Introduction

1.1 Motivation and Objectives

The Anatomic Total Shoulder Arthroplasty (TSA) is a surgical procedure that replaces the damaged glenohumeral joint with a prosthesis that recreates the anatomy and function of the normal shoulder. With a polyethylene (PE) component fixed at the glenoid and a cobalt-chromium component substituting the humeral head, the anatomic TSA is considered standard treatment for glenohumeral osteoarthritis (GHOA). The number of TSA has increased in the last two decades as the advance in prosthesis design and type has allowed its use in an increasing number of indications.

This procedure has been proven to be extremely successful in improving shoulder function and mobility and decreasing pain in patients with shoulder injuries that maintain the integrity of the rotator cuff—the rotator cuff consists of a set of muscles that work as active stabilizers of the shoulder joint and are essential to its good function [1]. However, although being a successful procedure in reducing pain and improving function in patients with shoulder injuries, TSA have a large number of complications that spoil its success. In fact, glenoid loosening corresponds to 80% of the long term complications that arise from anatomic TSA procedures [2]. Several mechanisms lead to glenoid loosening, including the failure of the implant itself, due to fracture or wear; lack of support of the underlying bone, due to low density regions, inadequate fixation, including cement failure and failure of the bone-cement interface. In 1988, Franklin et al. proposed the “rocking-horse” as a mechanism of glenoid loosening. This effect is associated with eccentric compressive loads that are applied on the glenoid surface and consequent humeral upward displacement, causing the glenoid component to tilt into a more superior facing direction [3].

FE analysis has been conducted to understand the influence of the implant design features on the joint stability, especially on the loosening of the glenoid component. Some parameters such as implant

geometry and material, orientation and positioning of the implant and component fixation have been analyzed in the literature to assess their influence on glenoid failure.

One other aspect that has been studied is the presence of a radial difference between the glenoid concave surface and the convex humeral surface. In fact, a number of authors have shown that the presence of this radial mismatch may decrease the risk of glenoid failure since conforming designs (equal radii of curvature) constraint humeral translation leading to eccentric loading [4]–[6].

Nevertheless, most of the studies addressing GH conformity and its influence on anatomic TSA outcomes are clinical and mechanical studies and finite element (FE) models studying this topic are scarce. Although a few studies refer an optimal mismatch interval, this topic is still something that is left to the judgement of the surgeon during the procedure [7]. Besides, it is still not clear in the literature what the influence of larger radial mismatches inside this interval is in the failure mechanisms of the glenoid component. Therefore, the implications of glenohumeral conformity is yet an understudied topic.

The objective of this study was to investigate the influence of joint conformity on the glenoid loosening mechanisms, through the analysis of glenohumeral translations, stress distributions on the cement and evaluation of the bone-cement interface of three different radial mismatches.

In order to allow for a better representation of the shoulder biomechanics, both abduction and flexion movements were analyzed for three anatomical configurations of the shoulder with respect to the radial mismatch between the humeral and glenoid components, as the real impact of this mismatch on the joint biomechanics is not yet completely understood. Three TSA were simulated considering 1, 3 and 5 millimeters radial mismatches. FE analyses were performed in Abaqus considering joint reaction forces estimated from a multibody model of the upper limb. The literature suggests that the implant failure occurs mostly at the bone-cement interface [8]. Therefore, two main analysis were performed: stress distributions on the bone cement were used to evaluate the probability of failure of the material; and the Hoffman criterion was used to assess the possibility of failure of the cement-bone interface.

1.2 Outline of the Thesis

This document is divided into six chapters. The current chapter, **Chapter 1**, introduces the reader to the overall problem that the thesis tries to answer as well as the overall structure of the work developed.

Chapter 2 presents the key concepts that are taken in consideration throughout this thesis. The anatomical aspects of the shoulder joint are described, focusing the bones, tendons and muscles that surround the joint. Moreover, the surgical procedure of the anatomic TSA is presented and the glenoid loosening mechanisms are discussed. Finally, previous computational models of the TSA are presented.

Chapter 3 describes the steps taken to develop this thesis, including the geometric modeling of the prosthesis, FE modeling and application of the multibody musculoskeletal model of the upper limb. The evaluation methods of implant failure are presented at the end of this chapter and include a detailed explanation of the Hoffman failure criterion.

In **Chapter 4**, the results of the multibody and FE models are depicted for all three configurations of the shoulder. These results are discussed in **Chapter 5**.

Finally, **Chapter 6** presents the main conclusions of this work as well as some considerations on future work.

Chapter 2

Concepts and considerations on Total Shoulder Arthroplasty

In this chapter, a few key concepts and considerations are described, including a short review of the anatomy of the shoulder complex, with focus on the structures that are involved on the TSA, Moreover, the shoulder replacement procedures will be explained with focus on the anatomic total shoulder arthroplasty and its components. Finally, a literature review is presented followed by the contributes of this thesis.

2.1 Shoulder joint

The shoulder complex is composed of three different bones, including the clavicle, scapula and the humerus and links the upper limb to the thorax. These bones articulate in four different joints: the glenohumeral (GH) joint, the acromioclavicular (AC) joint, the sternoclavicular (SC) and the scapulothoracic (ST) joint.

The pectoral girdle is suspended above the upper rib cage. It supports the arm and consists of two bones: the clavicle and scapula (Figure 2.1). The clavicle, or collar bone, is a long and slim, S-shaped bone that lies horizontally above the first rib and anteriorly to the thorax. The clavicle articulates with the sternum in its medial end and with the acromion of the scapula in its lateral end.

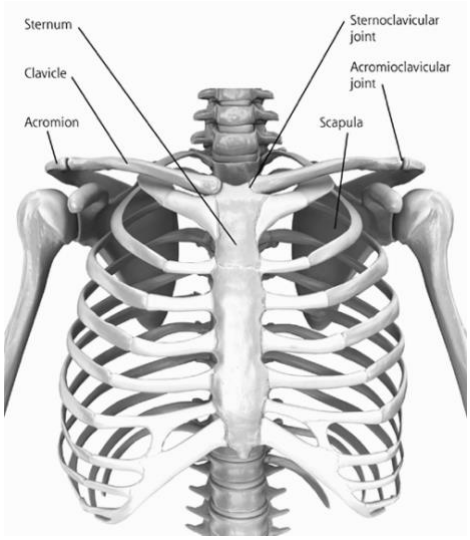

Figure 2.1: Joints of the shoulder girdle [9].

On the posterior part of the thorax is the scapula, which is a large, flattened, triangular bone. The three sides of the triangle are named superior, medial, and lateral borders, and its three angles are the superior, inferior, and lateral angles. The posterior face of the scapula has a sharp crest called spine that runs diagonally across the bone and divides it into two surfaces: the supraspinatus and infraspinatus fossae. The lateral end of this crest is the acromion, which articulates with the clavicle forming the AC joint. The anterior face of the scapula is slightly concave and consists of the subscapular fossa and the coracoid process, a projection of the scapula that allows for muscle attachment. On the lateral angle of the scapula, and inferior to the acromion, is the glenoid cavity, a shallow socket that articulates with the head of the humerus forming the GH joint. Attached to the margin of the glenoid cavity is the glenoid labrum, a fibrocartilaginous rim that deepens the originally shallow cavity, contributing for the stability of the joint [9]–[11].

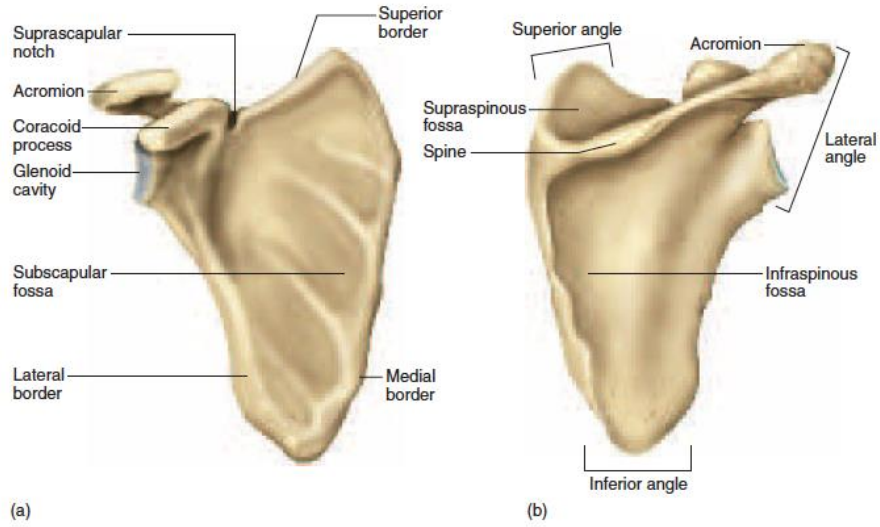

Figure 2.2: Anterior (a) and posterior (b) view of the right scapula [10].

The humerus is the longest bone of the upper limb and articulates with the scapula at the shoulder and with both the ulna and radius at the distal end. The most proximal part of the humerus is the head, which is spherical and forms the GH joint by articulating with the glenoid cavity of the scapula. Inferior to the head is the anatomical neck, which divides the humeral head from the greater and lesser tubercles, which are separated by the intertubercular groove. Inferior to the tubercles is the surgical neck, which is commonly susceptible to fracture. Distally to the surgical neck is the shaft of the humerus, a cylindrical-shaped site that contains the deltoid tubercle and the radial groove on its lateral and posterior aspects, respectively. In the most distal part of the humerus, there is an area called condyle that is composed of the trochlea, capitulum, olecranon, coronoid and the radial fossae (Figure 2.3) [11].

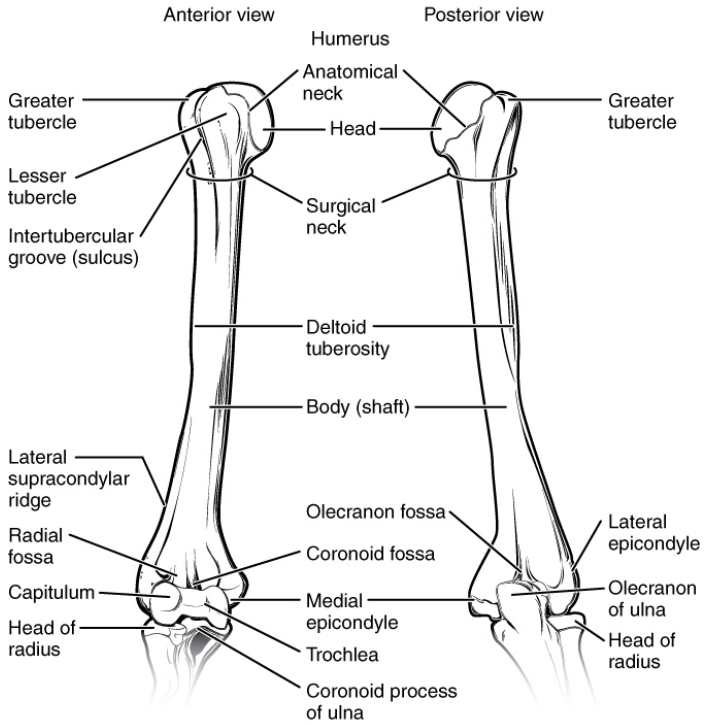

Figure 2.3: Anterior and posterior view of the humerus [12].

The glenohumeral joint is classified as a ball-and-socket joint and the mismatch between the head of the humerus and the glenoid cavity allows for a great range of movement, making it the most mobile joint in the body. This synovial joint is triaxial, allowing movements in three axis; therefore, the shoulder is capable of performing movements such as flexion–extension, abduction–adduction, and rotation.

As the inherent bony stability of the GH joint is limited, joint stability is essentially kept by the ligaments and muscles surrounding the joint. Five principal ligaments are involved in the stabilization of the shoulder joint: a set of three glenohumeral ligaments (superior, middle and inferior); the coracohumeral ligament; and the transverse humeral ligament. The glenohumeral ligaments originate from the humerus and converge toward the border of the glenoid labrum, limiting the external rotation of the humeral head. The coracohumeral ligament crosses from the coracoid process to the greater tubercle of the humerus,

while the transverse humeral ligament crosses between the lesser and greater tubercles of the humerus. Another stabilizer of the shoulder is the biceps tendon, which originates from the glenoid cavity border and passes through the joint capsule emerging into the intertubercle groove of the humerus. Here the tendon is clenched by the transverse humeral ligament, acting like a strap that keeps the humeral head against the glenoid cavity [10].

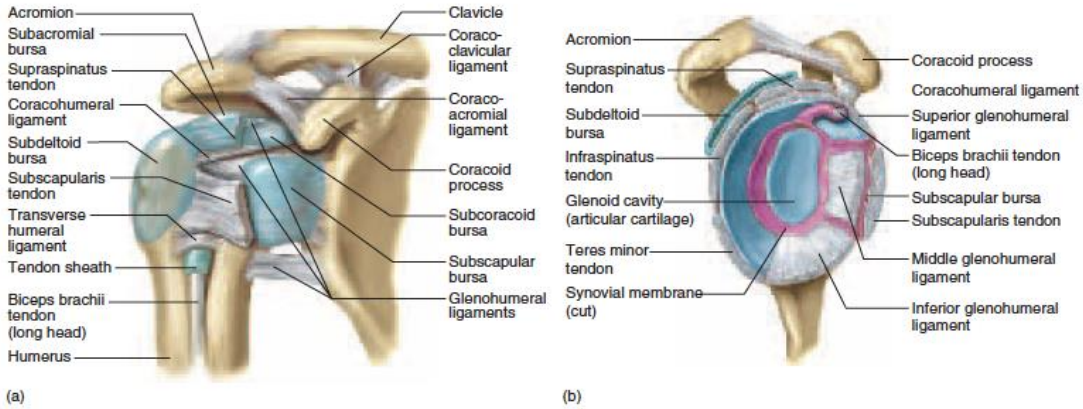

Figure 2.4: Anterior (a) and lateral (b) view of the ligaments and tendons of the glenohumeral joint [10].

Also contributing to the stability of the joint are four main muscles: the supraspinatus, infraspinatus, teres minor, and subscapularis, which are commonly called the rotator cuff muscles (Figure 2.5). The supraspinatus originates above the scapular spine at the supraspinous fossa and inserts on the head of the humerus. The infraspinatus originates on the infraspinous fossa and inserts at the posterior part of the head of the humerus. The teres minor originates at the lateral border of the scapula and inserts at the back of the head of the humerus, close to the infraspinatus. Finally, the subscapularis extends along the entire subscapular fossa converging into a tendon that inserts into the anterior part of the head of the humerus [9].

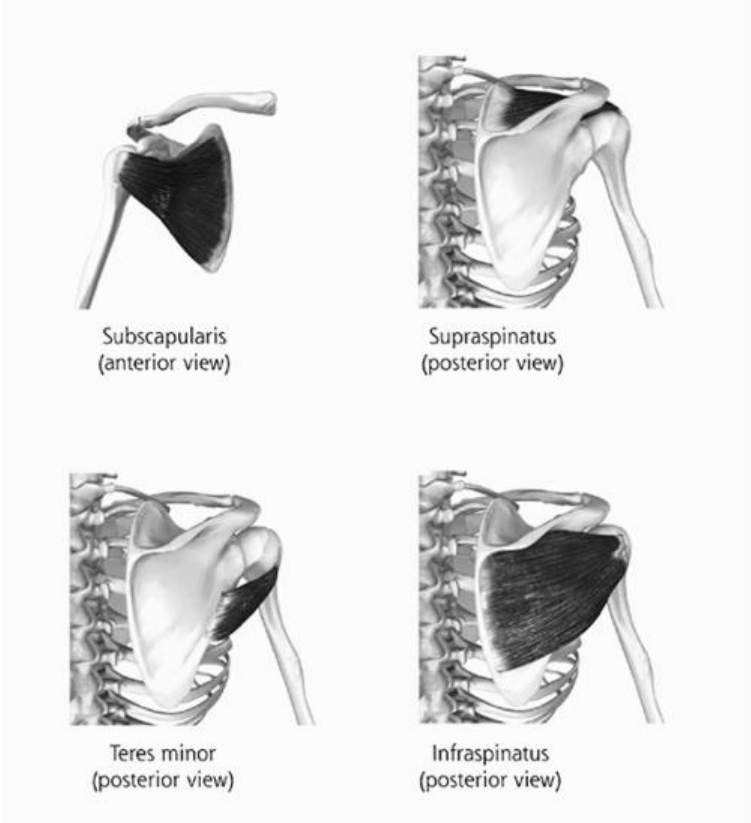

Figure 2.5: The rotator cuff muscles - subscapularis, supraspinatus, teres minor and infraspinatus [9].

2.2 Total Shoulder Arthroplasty

The shoulder joint is the most mobile joint in the body, and its function is a tradeoff between stability and mobility. When stability is compromised, due to anatomical variations or previous lesions, the risk of sustaining injuries increases, as an unstable shoulder accelerates the progression of joint pathologies and the need for surgical intervention.

Shoulder replacement surgery is one of the interventions that allow for a reduction of shoulder pain and dysfunction [1]. The most common arthropathy that leads to shoulder replacement is primary GHOA with degenerative changes, which occurs mostly in patients over the age of 60. On the other hand, secondary GHOA appears as a consequence of other conditions such as inflammation, osteonecrosis, rotator cuff tears, fractures or dislocations, and is also an indication for TSA since it leads to articular surface inconsistencies, followed by joint deterioration.

Nowadays, two types of total shoulder replacement surgeries are performed: the reverse and anatomic TSA (Figure *2.6*). The reverse TSA (Figure *2.6* (a)) inverts the ball and socket anatomy of the normal shoulder. This design places the spherical component into the place where the socket is and vice-versa. This medializes the center of the GH joint, changing the biomechanics of the joint, and preventing possible complications arising from a pathological rotator cuff. On the other hand, the anatomic TSA

(Figure *2.6* (b)) mimics the anatomy of the shoulder by replacing both glenoid cavity and humeral head with implants designed to copy the original shape and size of the structures being replaced.

The implant selection is made according to patient-specific factors. Although the anatomic TSA is extremely successful in treating GHOA, it is not advised for patients with rotator cuff deficiencies as it will most likely lead to implant failure and need for revision surgery. Contrarily, reverse TSA shows good results in patients with rotator cuff tears and proximal humerus fractures, and is usually used in revision surgeries for failed arthroplasties. Considering that this study focuses on the failure mechanisms of the glenoid component after an anatomic TSA, only this procedure is described in further detail hereafter.

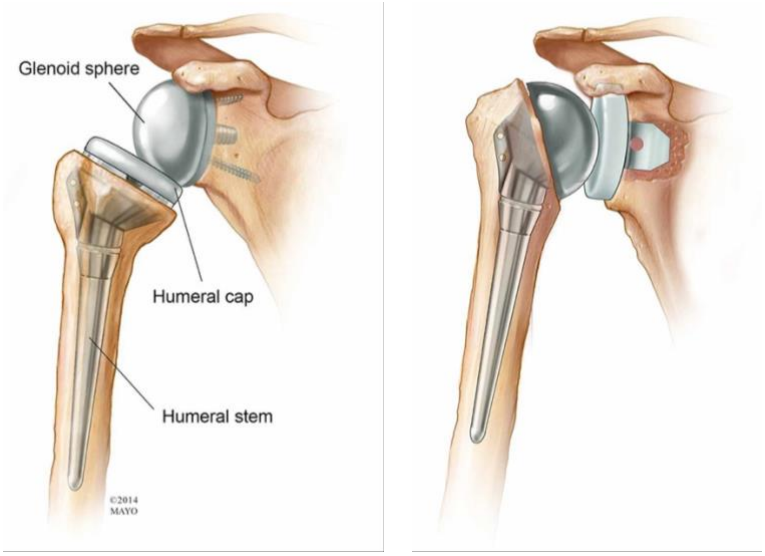

(a) (b)

Figure 2.6:Total shoulder replacements: (a) reverse total shoulder arthroplasty and (b) anatomic total shoulder arthroplasty [13].

2.2.1 Anatomic TSA

This subsection focuses on the anatomic TSA, its components, the underlying technique and possible complications. The anatomic TSA copies the anatomy of the healthy joint using two different components: the glenoid component, usually composed of ultra-high-molecular-weight polyethylene (UHMWPE), and the humeral component, composed of metal alloys.

2.2.1.1 Humeral Component

In 1951, Charles Neer published an article reporting 12 shoulder arthroplasties on patients with proximal humeral fractures. In his study, the arthroplasties reported corresponded to hemiarthroplasties, in which only the humeral heads were substituted by metal protheses [14]. Initially, the prosthesis' design was monoblock and stemmed; however, nowadays, a variety of humeral components are available, differing

in size and thickness. The current implants are generally modular, allowing for recreation of patient-specific anatomy and greater variability in height, inclination and humeral head offset [15].

One of the characteristics that has been changing over the years is the humeral stem. Although designs with large stems, as originally proposed by Neer, continue to be used, some novel designs present reduced stem lengths. Currently, three types of humeral stem components are available for anatomic TSA: standard-length stem, short-stem, and stemless implants.

(a) (b) (c)

Figure 2.7: Types of humeral components used in TSA: (a) Standard-length stem implant – DePuy Global® AP® System [16]*; (b) Short-stem implant – Tornier AEQUALIS ASCEND™ FLEX Convertible Shoudler Arthroplasty System* [17]*; and (c) Stemless implant – Tornier SIMPLICITI™ Shoulder system* [18].

The standard-length stem implant is inserted into the diaphysis of the bone either through press-fit or recurring to bone cement fixation. Complications following standard-length stem implantation include stress shielding and loosening of the component, leading to the need for revision. These factors have pushed the migration to short stemmed and stemless implants. The short stem implants allow for preservation of proximal humeral bone, which makes revision surgery easier if needed. This stem is incorporated at the metaphysis level, being less invasive while still providing adequate fixation [1]. The current trend in anatomic TSA is moving from short stems to stemless implants in order to minimize humeral bone removal and mimic the anatomy of the proximal humerus. The strong relation between stemless implants and proximal humerus anatomy improves the ease of the surgical procedure, especially when cutting and setting the implant in place.

2.2.1.2 Glenoid Component

In 1974, Neer introduced the first glenoid component. The design was made of PE, had a keel, and was fixed into the bone with bone cement [19]. The proposed implant had conforming humeral and glenoid

radii of curvature, meaning that both components had matching radii. Less than a decade after, in 1982, Neer was the first to report pain relief and improved shoulder function following TSA [20].

The importance and increased use of the glenoid component has incited its development and focus on its survivorship as failure of this component is considered the most common long-term complication of TSA. To provide good shoulder function and durability, at the time of surgery, the surgeon should take into consideration different aspects such as patient-specific anatomy, bone stock preservation and restoration of the joint line. Therefore, over the past years divergent implant designs and materials have been used in different configurations. The most common, and widely used, glenoid protheses include the cemented all-PE and the uncemented metal-backed (MBG) implants (Figure 2.8) [21].

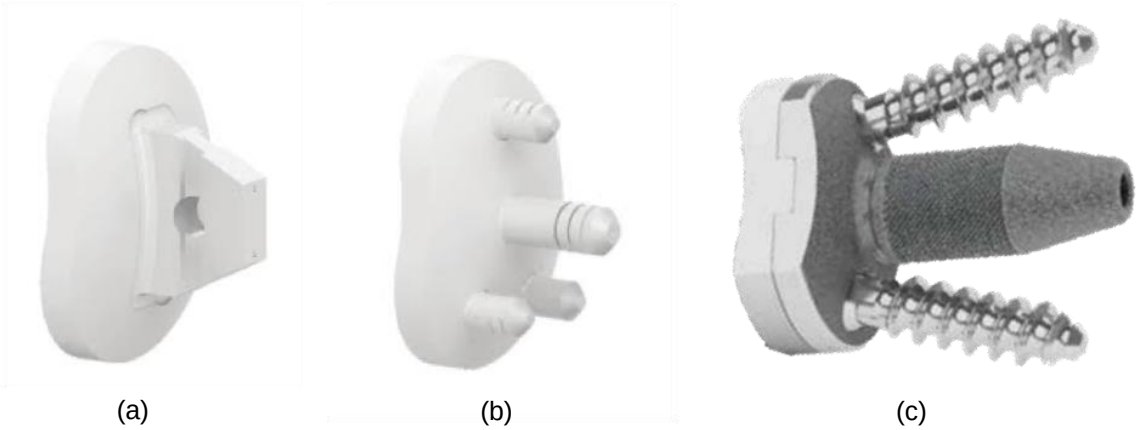

(a) (b) (c)

Figure 2.8: Design of different glenoid components: (a) keeled and (b) pegged all-polyethylene AEQUALIS™ PERFORM Anatomic Glenoid System ™ [22]*; and (c) Metal-backed SMR Anatomic by Lima Corporate (adapted from* [23]*)*

The all-PE prosthesis has seen different variations in the last years, in conformity/non-conformity, shape and keeled/pegged fixation. Moreover, the back of the glenoid component may be flat or convex; however, the latter appears to be more resistant to micromotions than the flat-backed designs.

Finally, the PE implant may either have pegs or keels to allow for fixation at the glenoid. The implant presented by Neer was keeled, and despite presenting an acceptable lifespan, it still failed to perform at the long-term, as the rate of radiographic loosening was high. The pegged components were designed to decrease the amount of subchondral bone removed and take advantage of the stronger peripheral bone for fixation of the glenoid implant. Besides, the cement used in the fixation of the pegged component is estimated to be 17% less than the amount used in the keeled design. This is important since the curing of the cement triggers an exothermal reaction that releases heat in proportion to the volume of cement. Therefore, this reduction in volume may reduce the risk of implant loosening as it lowers the likelihood of osteonecrosis, strongly associated with radiolucency [24].

The MBG implants are composed of two parts, a metal back and a PE insert (Figure 2.8 (c)). These implants are theoretically promising when it comes to glenoid fixation improvement and radiolucency

reduction. Actually, an uncemented fixation with tissue ingrowth or porous coating has been designed to increase implant stability and durability. Contrarily to the cemented fixation, if the immediate post-operative fixation is strong in an uncemented prosthesis, this strength should only increase with time as bone ingrowth improves implant longevity. Nevertheless, the results of these implants have not been encouraging as glenoid loosening was prevalent in a high percentage of patients before the 10 years mark after surgery [25].

The longevity of glenoid components has been improved over the years due to the evolution in biomechanics and design, however, the development and improvement of glenoid protheses are still far from over [21].

2.2.2 Surgical Technique

Every anatomic TSA must be adapted to the patient-specific anatomy. Besides, soft tissue balancing is a key step towards a successful TSA and includes tendon lengthening and capsular releases. In fact, during the exposure of the GH joint, after incision, the subscapularis tendon must be released as well as the joint capsule. If the surgeon fails to release the capsule from the humeral neck, it will complicate the dislocation of the humeral head away from the glenoid fossa.

Once the surgeon gets to the humeral head, it must be resected to allow the placement of the implant. Before the resection of the head, the surgeon must verify its diameter and thickness using a flat head gauge (Figure 2.9 (a)). Then, the humeral head sizer must be assembled to find the center of the head and the plane of the anatomical neck (Figure 2.9 (b)).

Once the center is found, a long threaded pin must be drilled into the humeral head, and should penetrate the lateral cortex of the humerus to block the migration of the pin in the cancellous bone (Figure 2.9 (c)).

Finally, the resection guide can be placed and the humeral head can be resected by inserting an oscillating saw through the guide. In the end, the head must be measured again to confirm the humeral head selection (Figure 2.9 (d))..

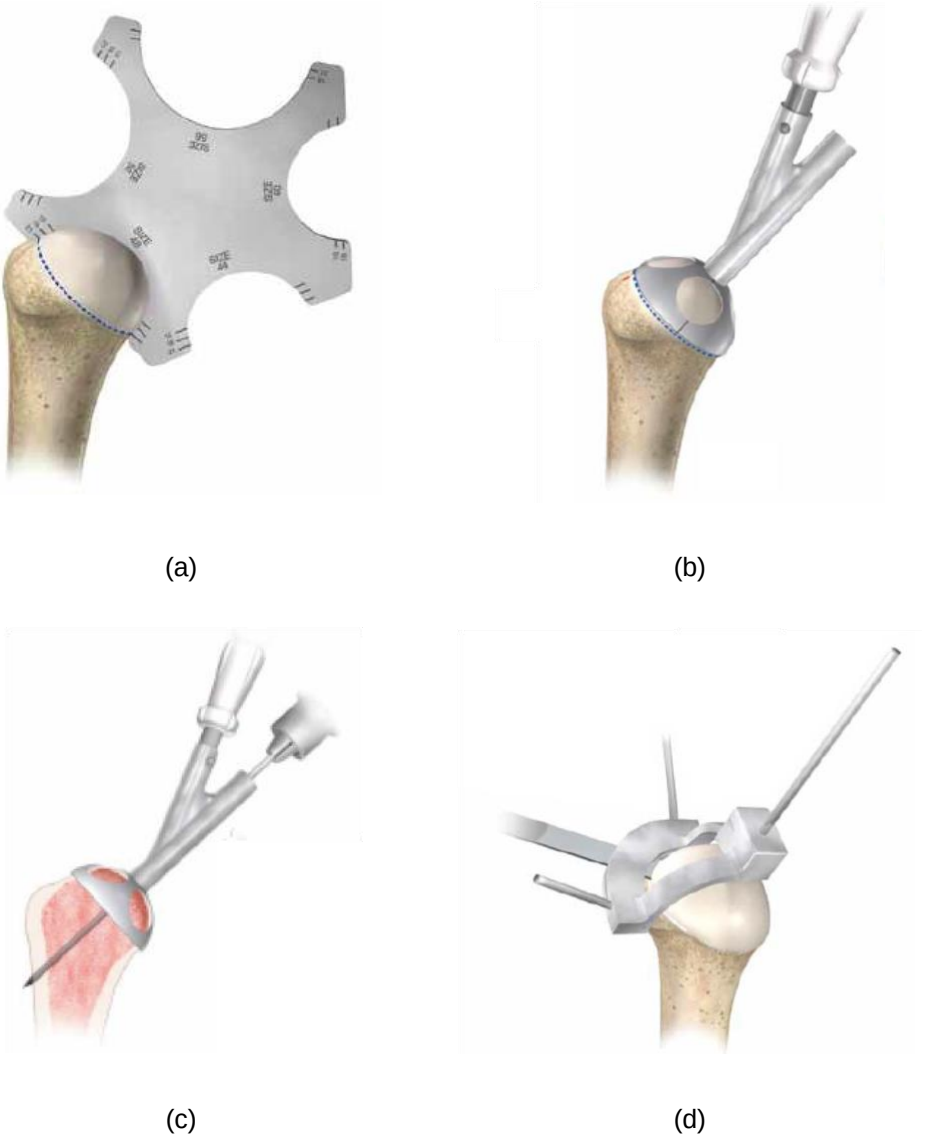

Figure 2.9: Surgical steps to perform the humeral head resection. (a) Use of the flat head gauge to assess the diameter and height of the head; (b) assembly of the head sizer followed by (c) placing of the center pin and (d) resection of the humeral head [16].

After cutting the humeral head, the humeral canal can be prepared to receive the implant's stem, if necessary. The tip of the reamer must be placed at the most superior point of the humerus and ream the medullary canal in line with its axis (Figure 2.10 (a)). A broach must be placed into the proximal humerus to act as a trial stem in order to ensure proper positioning of the stem and head trials and correct translation to the final implant (Figure 2.10 (b)).

(a) (b)

Figure 2.10: (a) Humeral canal preparation, (b) Broach/trial stem insertion [16].

After the preparation of the humerus, its osteotomy surface must be covered with an osteotomy cover to avoid damaging the proximal humerus. After this, the glenoid cavity of the scapula must be prepared for glenoid implantation.

The first step of glenoid preparation includes sizing and pin placement at the center of the glenoid (Figure 2.11(a)). The selection of the correct size glenoid is very important since the sizing disks determine the size of the glenoid implant, that determines the size of the humeral head. The sizer disk helps determine the center of the glenoid fossa. A hole must be drilled in the center of the glenoid cavity to place the pin. The pin is then attached to a spherical reamer of adequate size and the reaming of the glenoid surface is performed (Figure 2.11(b)). However, over-reaming of the glenoid reduces both the area of the glenoid face and the depth of the glenoid vault, and thus should be avoided.

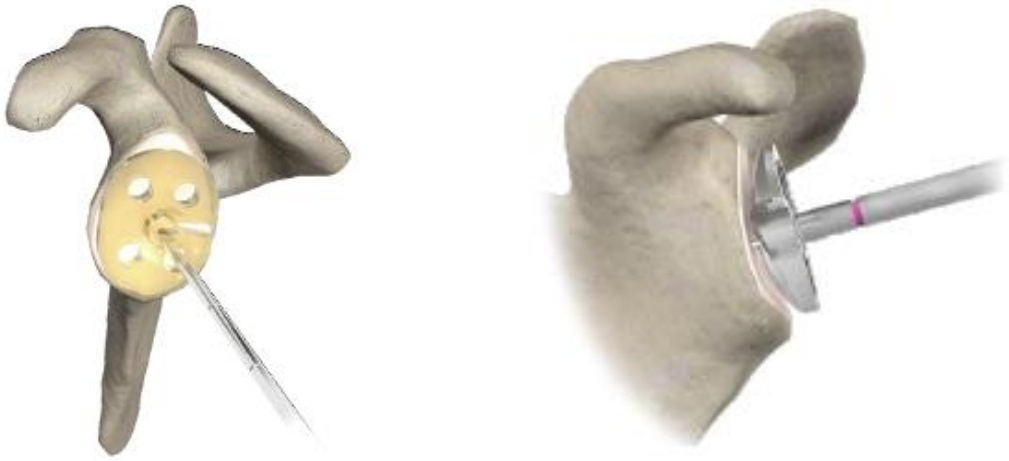

(a) (b)

Figure 2.11: Glenoid preparation for implantation. (a) Sizer disk and guide pin for center identification; (b) glenoid reaming using spherical reamer inserted into the guide pin [25].

After preparing the glenoid, trialing of the glenoid implant is necessary in order to determine the correct size for the implant. The trial should perfectly sit on the surface of the bone, with full and concentric contact between its back and the reamed surface of the scapula (Figure 2.12). If the fit is not adequate, some of the previous steps regarding bone preparation must be repeated.

Figure 2.12: Glenoid trial to confirm the fit between the implant and the bone [16].

In this study, an all-PE, 4 peg glenoid prosthesis is analyzed. For this kind of implant, three holes must be drilled to accommodate the three peripheral pegs (Figure 2.13). The central, anchor peg is press-fit and is covered with a morselized bone paste put together during glenoid reaming and drilling. This allows for better tissue integration and, consequently, for better fixation of the glenoid component as seen in Figure 2.14.

(a) (b)

Figure 2.13: (a) Peripheral peg drilling; (b) recommended order of peripheral peg hole preparation: 1) anterior-inferior 2) anterior- posterior 3) superior [26].

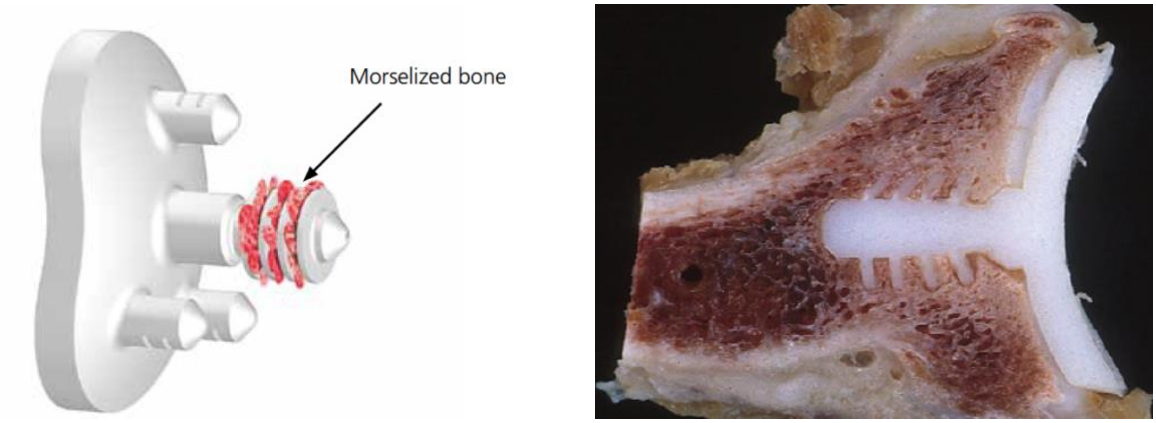

(a) (b)

Figure 2.14: Anchor peg system: (a) Central anchor peg covered with morselized bone paste [16] *and (b) tissue integration surrounding the central anchor peg in vivo* [27].

Before glenoid implantation, the bone cement is placed inside the peripheral holes. It is important to ensure that there is no significant cement excess extruding from the holes, as this may create an uneven cement mantle between the PE and bone, leading to damage and loosening of the glenoid component. Finally, the glenoid may be implanted and the glenoid aspect of the procedure is concluded. After this, the osteotomy protector of the humerus should be removed and the focus must return to this structure.

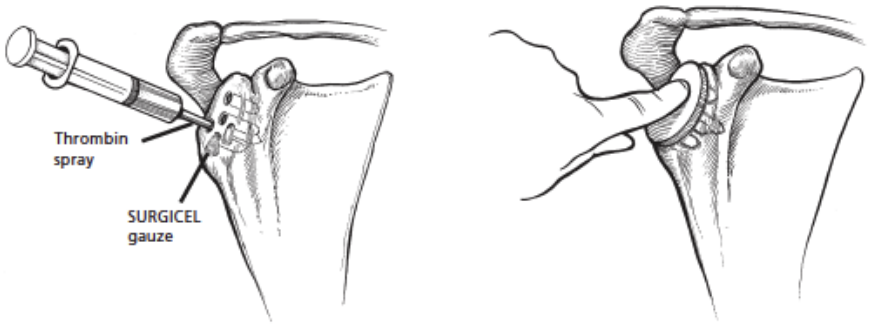

Figure 2.15: Cement placement on the drilled peripheral holes (on the left) and final glenoid implantation (on the right) [28].

The trial of the humeral head must take into consideration both the size of the resected humerus as well as the size of the glenoid implant chosen. According to DePuy's surgical procedure catalog, the radial mismatch between the humeral head and the glenoid must be 1, 3 and 5 millimeters. Figure 2.16 shows a glenohumeral mismatch of 3mm (6mm diametral mismatch). To obtain different mismatches the manufacturer recommends increasing or decreasing the size of the humeral component.

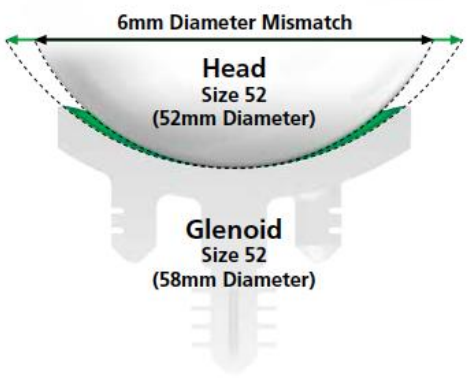

Figure 2.16: Glenohumeral mismatch of 3mm [16].

After choosing the appropriate size of the humeral trial and confirming it with reduction of the shoulder, the trials of both the stem and the humeral head may be replaced by the final implant.

2.2.3 Complications

Regardless of its evolution over the years, the TSA outcomes are still far from perfect, presenting complication rates of 10.3% [29]. The most common complications include loosening of the components, periprosthetic fractures, glenoid wear, rotator cuff tears, joint instability, neurologic injuries and infection. In 2017, Bohsali et al. [29] reviewed all complications of anatomic TSA reported in studies from 2006 to 2015, stating that component loosening following TSA made up 39% of the post-surgical complications, with approximately 38% corresponding to glenoid loosening and only 1% corresponding to humeral component loosening. Moreover, the second highest incidence rate was for glenoid wear, which

corresponded to 22.6% of all complications, followed by shoulder instability, with an incidence of 10.1%. Shoulder instability has been associated with component malpositioning and rotator cuff lesions that change the joint biomechanics and kinematics. Glenohumeral instability can be sorted into superior, anterior and posterior instability. While the first is usually connected to rotator cuff deficiencies, it can also be associated with an injured coracoacromial ligament. On the other hand, anterior instability may be caused by implant malpositioning, with excessive anteversion of the components, or subscapularis lesion, resulting from incorrect sizing of the humeral head (excessive humeral size may lead to muscle rupture) or from poor tissue quality. Finally, posterior instability is caused by posterior capsule laxity or excessive implant retroversion [29], [30]. Additionally, rotator cuff tears were present in 9% of the shoulders analyzed, while periprosthetic fractures had an incidence of 6.7%. Finally, neural injury and infection accounted for 6.1% and 4.9% of all complications after TSA.

2.2.3.1 Glenoid loosening mechanisms

The loosening of the glenoid component is the most common complication in patients following TSA and is responsible for the greatest share of unsatisfactory outcomes after this procedure [31]–[33]. The failure of this component is clinically related to arthralgia and function impairment [34]. The glenoid component can fail through different mechanisms; however, it is normally a result of its inability to mimic the key properties of the original joint when it comes to the fixation to the underlying bone, resistance to cyclic eccentric loading, and GH translation [35]. Glenoid loosening is usually visible through radiolucent lines in medical imaging of the shoulder.

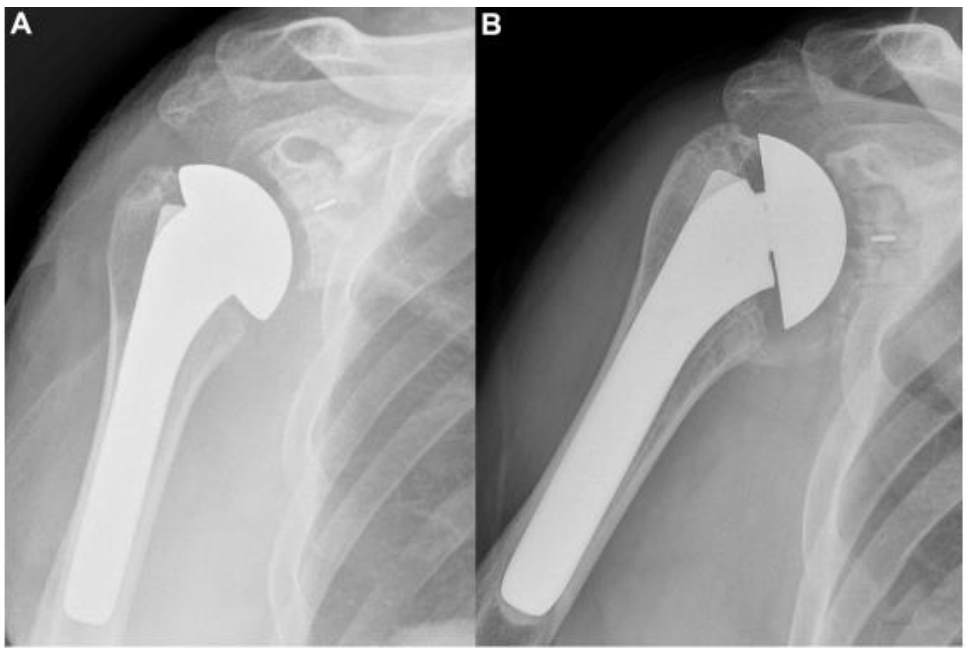

Figure 2.17: (A) Early postoperative x-ray of the shoulder. (B) 5-year postoperative x-ray of the GH joint with lucency around the all-polyethylene implant [36] .

The risk of failure, however, depends on the design of the glenoid implant - keeled glenoid implants carry a higher risk than pegged ones [37] and MBG implants have a higher failure rate than all-PE implants [38].

The failure mechanisms of the glenoid include the failure of the component itself, lack of bone support, inadequate fixation and eccentric loading followed by the rocking horse effect. The glenoid component may fail due to periprosthetic fracture and wear of the implant surface [39], [40]. Moreover, the lack of support from the underlying bone may also contribute to glenoid loosening and can occur due to over reaming of the glenoid cavity, with excessive removal of bone, and due to the negative adaptation of the bone in the presence of the implant due to stress shielding [32], [41]. Additionally, the inadequate fixation of the glenoid component allows it to move in relation to the scapula, decreasing stability and increasing the risk of total failure of the interface. The inadequate fixation may be caused by a suboptimal cement technique, which leads to the reduction of the component's capacity to resist the lift-off effect caused by eccentric loading. Besides, the failure of the cement material due to excessive loading also leads to the failure of the fixation.

The eccentric loading of the glenoid challenges all involved components, i.e., the PE component, bone cement, and bone. The loading at the rim of the glenoid associated with component malposition, inferior positioning of the glenoid, often lead to a phenomenon called the rocking-horse effect, which is yet another mechanism of glenoid loosening.

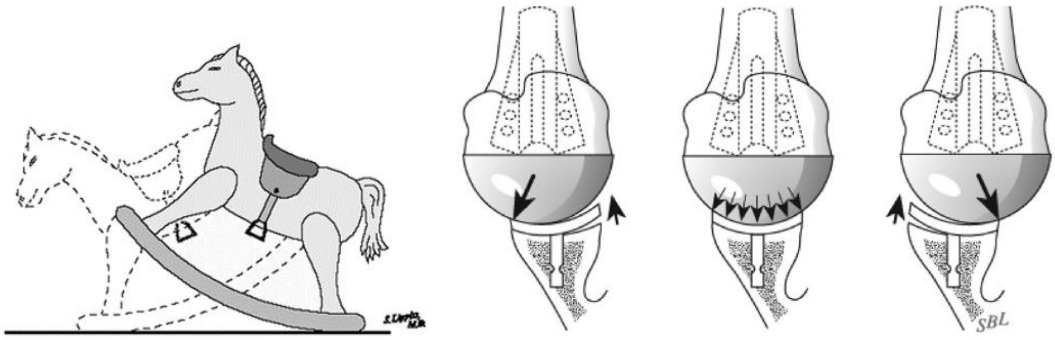

Figure 2.18: Rocking-horse phenomenon described by Franklin et. al. [3] *as a result of eccentric loading and humeral head translation on the glenoid* [42].

The rocking-horse phenomenon was firstly described in 1988 by Franklin et. al. [3] as the main cause of glenoid loosening and implant failure after TSA. This effect is often associated with rotator cuff deficiency, since the dynamic stability provided by these muscles is compromised, leading to eccentric loading of the glenoid. Previously, in 1983, Neer et. al. had described the impact of cuff deficiency on the kinematics of the glenohumeral joint as an upward translation of the humeral head in relation to the glenoid, towards the acromion [43]. The eccentric compressive loading of the glenoid, together with the superior translation of the humerus described by Neer, forces the glenoid implant to tilt and face a more superior direction. As the humeral head moves to a superior and inferior direction, it generates a lifting

effect on the opposite side of where the humerus is moving, which mimics the function of a rocking-horse.

2.2.4 State of the Art

This section provides a review of previous computational studies addressing both the biomechanics of the shoulder joint and the TSA. Computational models of the shoulder can be roughly divided into two categories: multibody models and FE models. On the one hand, multibody models are generally used to estimate muscle and joint reaction forces. These models are based on rigid body dynamics, where bodies are assumed to be rigid and cannot undergo deformation, and muscles are reduced to single line actuators [37, 38]. This type of model has the ability to evaluate musculoskeletal dynamics, but, due to the great simplifications, it fails to simulate the intricate stress distributions and interactions of the different structures of the shoulder complex, which are key components of the physiological and biomechanical joint function [46]. On the other hand, FE models allow the evaluation of a number of variables that are not accessible through multibody modeling, such as the internal loading conditions and stress and strain distributions in all tissues. The FE method begins with discretization of the computational domain into a finite number of elements, which are smaller components with simple geometry (e.g. triangle in 2D or tetrahedron in 3D). The next step is to find individual solutions for each element that satisfy the differential equation within its boundary. By gathering the local solutions of all elements, a global solution can be derived, allowing complex nonlinear problems to be solved numerically [37,41]. The use of this powerful tool, in investigation on scientific fields such as biomechanics and orthopedics, has been increasing in the last decades, being a key contributor to the understanding of tissue structure and improvement of the design of orthopedic implants [48]. In fact, FE analysis is being used to address a broad range of GH joint problems and conditions such as overall joint stability, rotator cuff tears and glenoid capsule and labrum defects [43–45]. Regarding TSA, FE analysis has provided insight into the influence of implant design features on the joint stability, especially on the major clinical issue of glenoid loosening.

The design parameters covered in the literature include implant geometry and material, orientation and positioning of the components and fixation methods (cement/uncemented glenoid fixation).

The geometry of the glenoid implant has been analyzed in several studies. Lacroix et. al. conducted a 3D FE analysis for two different glenoid designs, keeled and pegged, for both heathy and rheumatoid arthritis conditions [52]. They found that for healthy conditions the pegged fixation method outperformed the keeled design, while for a rheumatoid bone the keeled implant was more suitable. To predict the percentage of cement at risk of failure, a maximum-principal stress based failure model was used. It was predicted that the percentage of bone cement with a survival rate higher than 95% in the pegged design was 94% versus 68% in the keeled design in healthy conditions. However, in rheumatoid bone, the scenario changed—the results for the pegged implant decreased to 86% whereas those of the keeled design increased to 99%.

The influence of glenoid positioning on the scapula has been studied to understand the optimal position for the glenoid that avoids premature glenoid loosening. A recent FE study [53] evaluated the influence of the glenoid implant depth on the mechanics of the bone-cement interface and confirmed the hypothesis of maximum bone stock preservation. The results showed that for deeper implants, the amount of cortical bone retrieved during reaming was higher than that of more shallow implant. Moreover, the stresses within the bone cement steadily increased with increasing implant depth, concluding that the deeper the implant, the higher the probability for the fatigue stress of the bone cement to be exceeded.

The inclination of the glenoid component was addressed by Karelse et. al. [54] who evaluated the shear forces in two glenoid positions. These positions were defined by two planes, the maximum circular plane (MCP) and the inferior circular plane (ICP). The MCP was defined by the best fitting circle of three points along the glenoid rim, the most superior and two points at the inferior part of the rim. Moreover, the ICP was defined as the best fitting circle of three points on the rim that correspond to the inferior quadrants. The inclinations of these planes in relation to the intersection with the scapular plane averaged 95º and 111º, respectively. The results showed that in early abduction, the component placed in the MCP was subject to significantly higher shear forces than that placed in the ICP, concluding that the latter positioning of the glenoid might decrease the threat of the rocking-horse effect.

Hopkins et. al. [55] studied five different glenoid alignments (central, anteversion, retroversion, superiorly inclined and inferiorly inclined) to assess their influence on negative clinical outcomes related to the failure of the bone cement. The FE study of the central aligned glenoid had better results for unloaded abduction when compared to the anteversion and retroversion models, and the anteverted alignment performed better than the retroverted glenoid. Moreover, the study concluded that a misalignment in the superior-inferior direction was less likely to undergo mechanical failure than that in the anterior-posterior direction.

The fixation of the glenoid component onto the scapula has also been the focus of some studies found in the literature. The perception behind the use of bone cement has been changing as several studies suggested that MBG implants might be better than cemented components [47–49]. However, biomechanical and clinical studies have shown a worse performance of MBG implants when compared to cemented implants. In fact, Quental et. al. [41] have shown that the stress shielding phenomenon is more intense in uncemented designs (cementless and MBG implants) than in all-PE cemented components, with poor bone adaptation in MBG implants. Therefore, the researchers concluded that the cemented implants are more likely to resist to aseptic loosening of the glenoid component. Moreover, Terrier et. al. [8] assessed the impact of the cement thickness on the bone-cement interface and corresponding glenoid loosening and found that the stresses in the cement increased when its thickness decreased, setting the optimal cement thickness at 1.0 to 1.5mm to avoid cement fatigue and interface failure.

The glenohumeral conformity is another topic that has been discussed in the literature regarding its influence on stress distributions and glenohumeral translations. The optimal radial mismatch between the glenoid and humeral head components is yet to be determined for cemented all-PE pegged implants;

nevertheless, a recent mechanical study has suggested that a radial mismatch lower than 10mm may decrease the risk of glenoid loosening by reducing the risk of glenoid micromotion related to the rocking-horse effect [7]. Although conforming designs allow for greater stability than non-conforming designs, since the humeral head is perfectly fitted into the glenoid cavity, they also carry the risk of eccentric loading in the course of humeral translation over the glenoid. The presence of a mismatch allows for the humerus to translate at the expense of reducing contact area, which increases the possibility of PE failure due to increased contact stresses. Zhang et. al. evaluated the stress distribution in three different TSA configurations with different glenoid designs, a conforming, a non-conforming and an hybrid design [59]. The study showed that the maximum Von Mises stress at the superior region of the glenoid was higher in the conforming design than in the other two, and was also higher than that in the central and transitional regions of the glenoid for all three configurations. Lacroix and Prendergast [56] developed 2D FE element models of keeled glenoid designs and found that, compared to non-conforming designs, a higher conformity allowed for more moderate stresses in the cement. Despite the contribution of these studies to the body of knowledge, the influence of the glenoid articular conformity on the failure mechanisms of an all-PE pegged implant under physiological conditions is yet to be established. Therefore, this subject is the focus of this study.

2.3 Contributions of this thesis

Despite being the most common complication after TSA, the influence of implant design on glenoid loosening mechanisms is still not completely understood. To the author's knowledge, no studies have evaluated the influence of the components' radial mismatch in the glenoid loosening mechanisms using FE analysis and under physiological loading, retrieved from multibody models. This study allows for a better understanding of the impact of articular conformity in the failure mechanisms of the glenoid in realistic conditions taking into consideration the failure of both cement and bone-cement interface.

Chapter 3

Materials and Methods

This chapter presents the methodologies followed in this thesis (Figure 3.1), from implant design and virtual implantation to an in-depth description of the FE model used and the different cases in analysis. The different software used throughout this study are depicted in Table 3.1 along with the steps in which they were used. The procedures followed for the evaluation of results are presented at the end of this chapter.

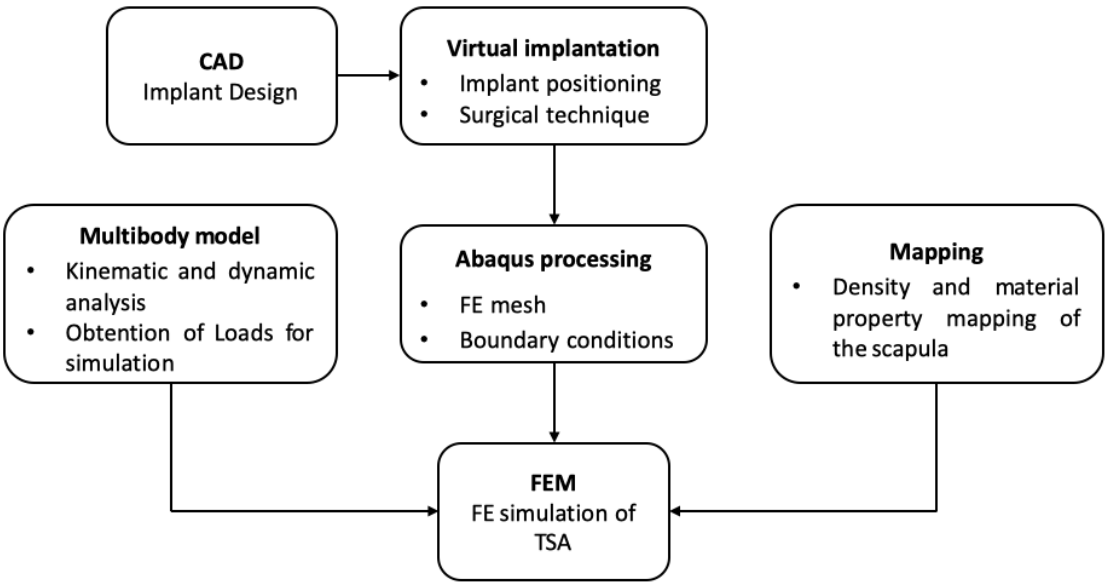

Figure 3.1: Methodology used to study the failure mechanisms of the glenoid component after anatomic TSA.

Table 3.1: Software used to develop the FE models used to study the failure mechanisms of the glenoid component after anatomic TSA.

Purpose	***Software***	***Distributor/Manufacturer***
CAD / Implant Design	*SolidWorks*	Dassault Systèmes
Multibody model	*Matlab*	MathWorks Inc
Density Mapping	*Matlab*	MathWorks Inc
FE analysis	*Abaqus*	Dassault Systèmes

3.1 Geometric modeling of TSA

3.1.1 Glenohumeral joint

The glenohumeral joint model, shown in Figure 3.2, was provided by the research group in which this project was developed [41], [60]. It corresponds to the right shoulder of a male and was obtained through the computational processing of CT data.

Figure 3.2: Glenohumeral joint model provided by the research group .[60]

3.1.2 Implant Model

The computational model of the implant was designed in *SolidWorks* and was based on the Global APG Shoulder System (Anchor Peg Glenoid) design from DePuy. This system is divided into glenoid and humeral components.

3.1.2.1 Glenoid component

The glenoid prosthesis used in this study was a 4 pegged, convex back, all-PE implant (Figure 3.3). The dimensions of the implant used are depicted in Table 3.2 and were obtained from pegged glenoid implant of the Titan™ Modular Shoulder System, 2.5, due to scarce information on the DePuy's implant size and design similarity between the two implants [61]. The dimensions were chosen according to the properties of the studied GH joint. To study different mismatch configurations, the glenoid was left unchanged, while the humeral head radius was changed [62]. The radius of the glenoid implant was chosen according to the same catalog, and adapted to the size of the glenoid in study, being fixed at 27mm.

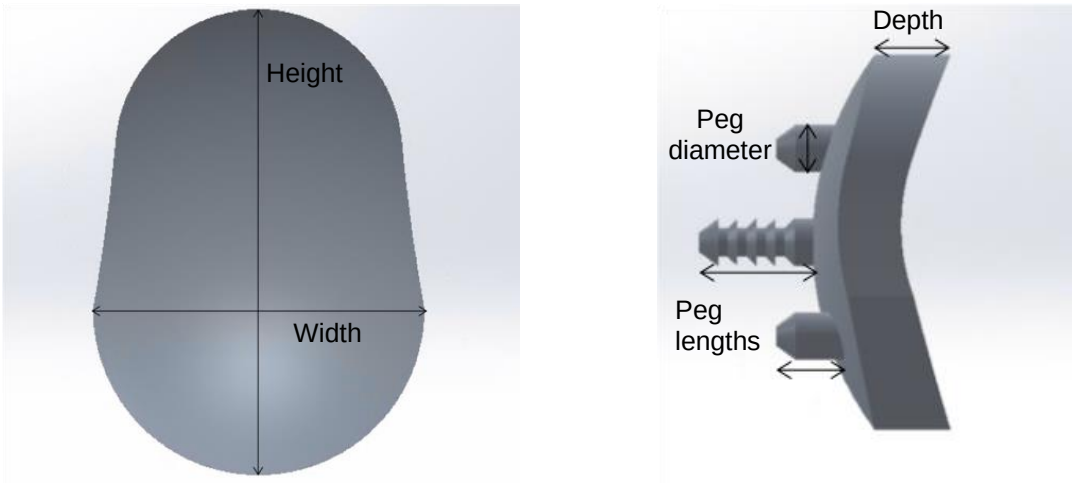

(a) (b)

Figure 3.3: Sagittal (a) and frontal (b) view of the glenoid implant designed.

Table 3.2: Glenoid dimensions used in implant design [61].

Height	*39.4mm*
Width	28.9mm
Depth	6mm
Central peg length	15.2mm
Peripheral peg length	6.4mm
Peg diameter	5mm

The implantation of the glenoid component followed the surgical technique from DePuy Synthes [28] and included the reaming of the glenoid cavity for bone preparation. The reaming of the glenoid was made with the help of a guide pin (central hole to define center of the glenoid fossa) and a spherical reamer with the same radius as that of the glenoid implant (Figure 3.4).

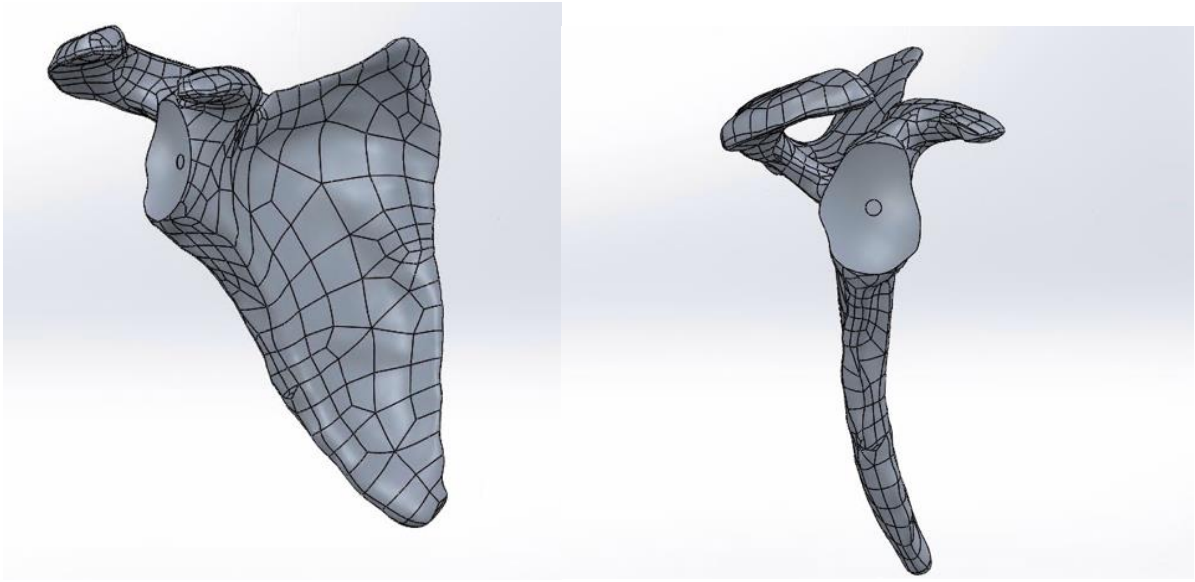

Figure 3.4: Scapula after glenoid reaming for bone preparation.

For glenoid fixation, a cement mantle of 1mm [26] was modelled as depicted in Figure 3.5. The cement does not cover the central peg as this is an anchor peg that is covered in a bone paste from the bone retrieved during glenoid preparation. This helps facilitate tissue integration, improving implant fixation and, consequently, its survival time.

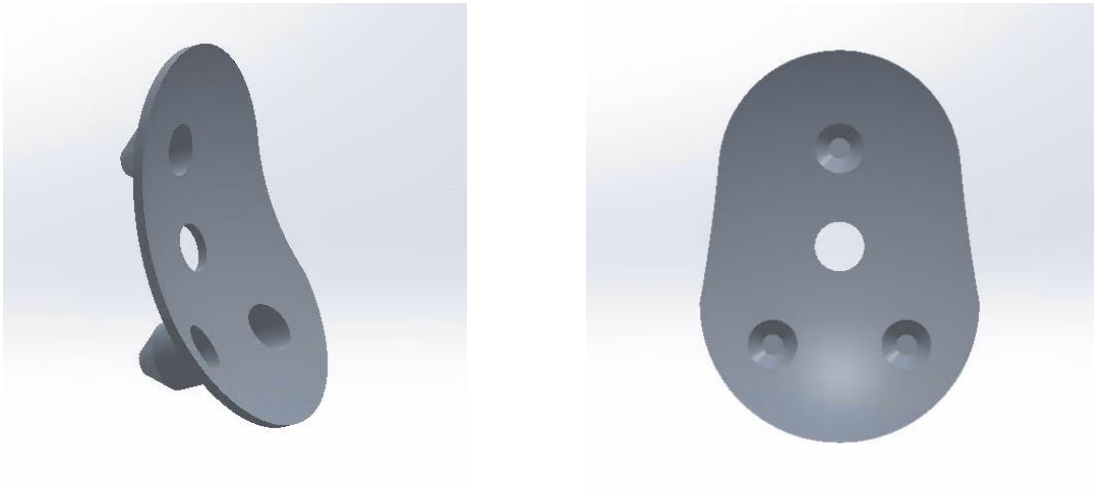

(a)

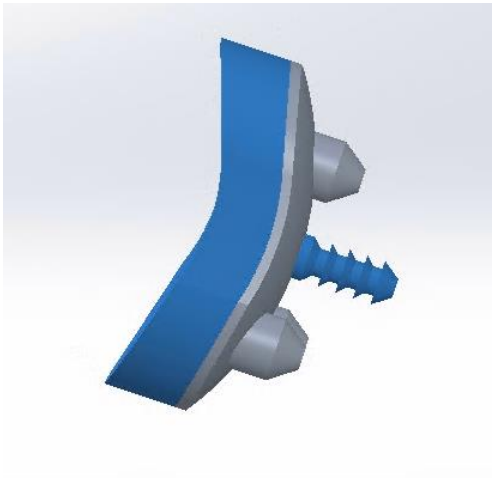

(b)

Figure 3.5: (a) Cement mantle for glenoid fixation and (b) glenoid-bone fixation.

Finally, the implant and cement were attached to the reamed bone to mimic the glenoid preparation and implantation during the TSA surgery (Figure 3.6).

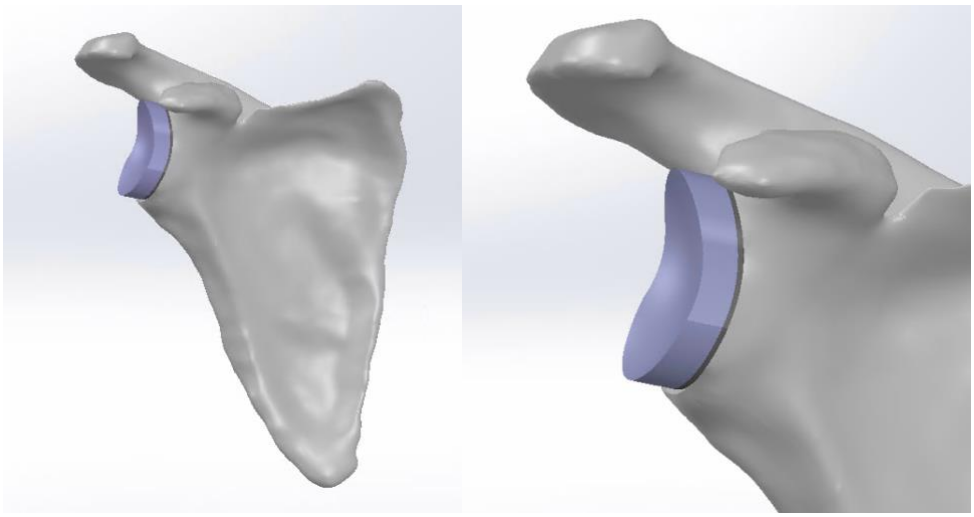

Figure 3.6: Glenoid component implanted in the scapula.

3.1.2.2 Humeral component

Three humeral components were modelled to define three radial mismatches. The radii used were 26mm, 24mm and 22mm to obtain mismatches of 1, 3 and 5 millimeters, respectively. The implant was designed as a cut semi sphere with 18mm of height according with the specifications in the DePuy surgical technique catalog. For the sake of simplicity, as it did not affect the aim of this study, the stem of the humeral components was neglected.

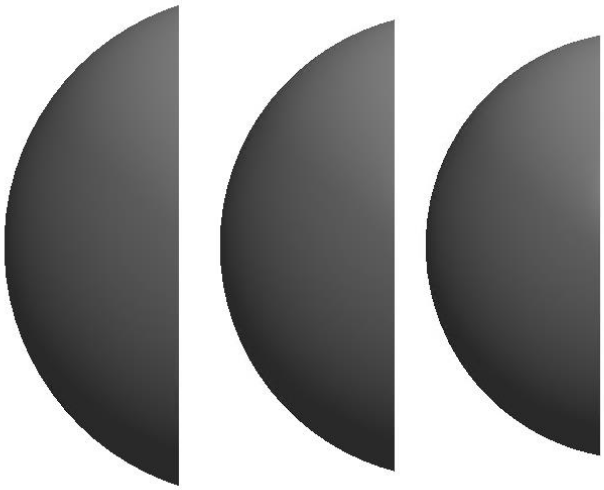

Figure 3.7: Humeral components for simulation of TSA with different mismatches. From left to right: 26mm radius, 24mm radius and 22 mm radius.

For the implantation of the humeral component, the humerus was cut according with the humeral head cutting guide (fixed at 135º) (Figure 3.7 (a)) to mimic the humeral resection described in the surgical technique catalog [16]. The humeral head was then placed onto the cut surface of the humerus as depicted in Figure 3.8.

(a) (b) (c)

Figure 3.8: (a) Humeral head cutting guide [16]*; (b) cut humerus for implantation and (c) implanted humeral head.*

3.1.3 TSA complete model

The final model was achieved by assembling all components, as shown in Figure 3.9. The different mismatches were applied only in the humeral head diameter as the rest of the model remained unchanged. The final configurations were approved by an orthopedic surgeon (Dr. Marco Sarmento

from Hospital of Santa Maria, Faculty of Medicine, University of Lisbon) and are presented in Figure 3.10.

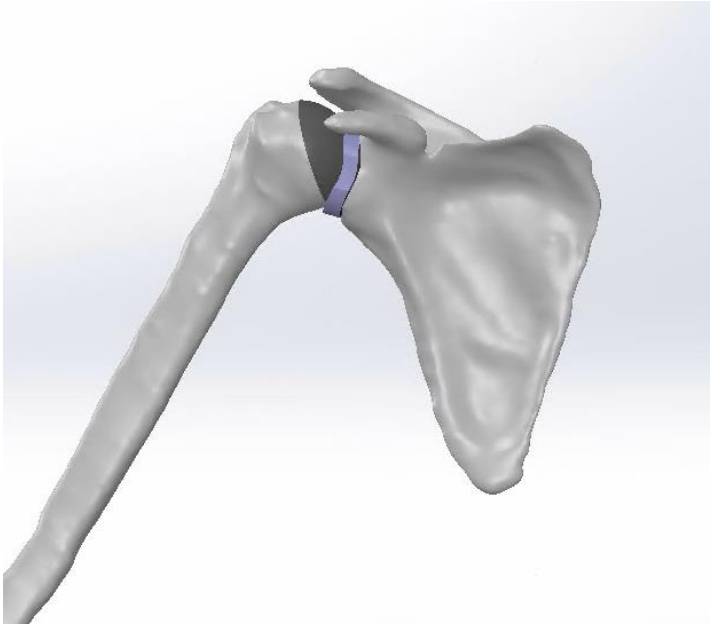

Figure 3.9: Final TSA model for 3mm radial mismatch.

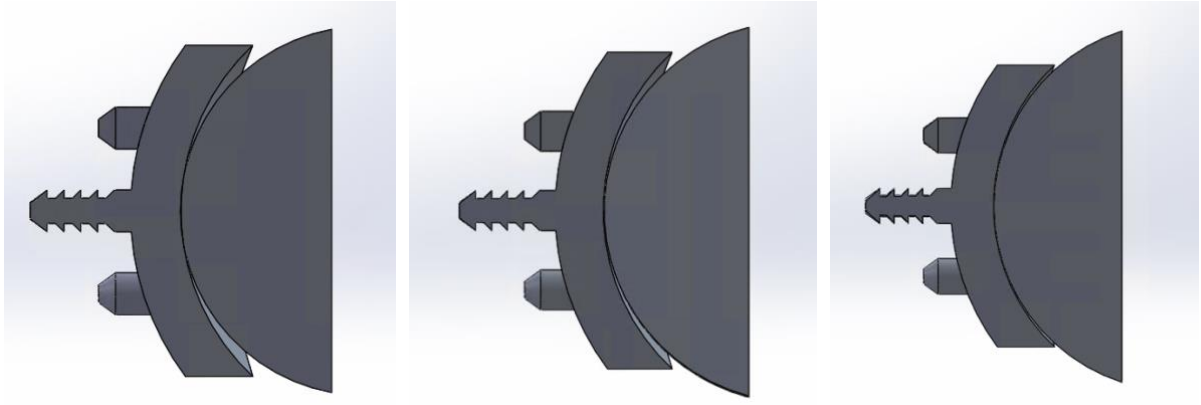

(a) (b) (c)

Figure 3.10: GH configurations for three TSA. (a) 5mm radial mismatch; (b) 3mm radial mismatch and (c) 1mm radial mismatch.

3.2 Multibody modeling of TSA

To estimate the kinematic and dynamic behavior of the shoulder joint, the musculoskeletal model of the upper limb developed by Quental et. al. [60] was applied. This model includes 7 rigid bodies, 6 anatomical joints and 21 muscles. The GH joint is modelled as a spherical joint with clearance, allowing

for the simulation of its 6 degrees of freedom. Muscle, joint reaction forces and GH translations are estimated using an inverse dynamics approach. In this study, abduction and flexion motions previously acquired at the Laboratory of Biomechanics of Lisbon were analyzed.

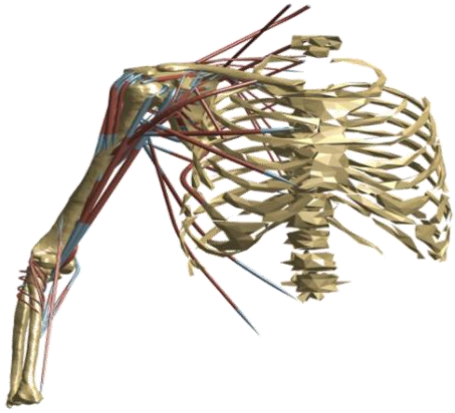

Figure 3.11: Muscoskeletal model used for defining loading conditions and analyzing GH translations [60].

To simulate the TSA configurations developed in Section 3.1, including different radial mismatches, the GH joint description was updated accordingly—the center of rotation and radius of the articular surfaces of the humeral and glenoid components, measured in Solidworks, were implemented in the musculoskeletal model of the upper limb, whose subject was the same as that of the computational model in Solidworks.

In the musculoskeletal model, the elastic force developed in the GH contact is described by a Hertz contact force model given by:

$$\begin{cases} F_N = 0, & \delta < 0 \\ F_N = K\delta^{1.5}, & \delta \geq 0 \end{cases} \tag{3.1}$$

where K is the generalized stiffness constant and δ is the relative normal deformation between the articular surfaces. The generalized stiffness was defined as

$$K = \frac{4}{3(\sigma_i + \sigma_j)} \sqrt{\frac{R_i R_j}{R_i + R_j}} \tag{3.2}$$

where R_i and R_j are the radii of the articular surfaces, and σ_i and σ_j are given by:

$$\sigma_k = \frac{1-\nu_k{}^2}{E_k}, (k = i, j). \tag{3.3}$$

In Equation (3.3), E_k is the elastic modulus of the material of component *k* and υ_k is its Poisson's ratio [63]. For the glenoid component, $E = 500MPa$ and a $\nu = 0.4$ were used, corresponding to UHMWPE, while for the humeral head, made of a cobalt-chromium alloy, $E = 230GPa$ and a $\nu = 0.3$, were used [53].

3.3 Finite element modeling of TSA

Three FE models were developed in Abaqus, one for each radial mismatch configuration. The development of these models involved different steps, such as the assignment of material properties to each component, meshing of all components, definition of contact and interaction properties between the components of the TSA, application of loads and definition of boundary conditions. The 3D geometric models of the TSA were converted from SolidWorks to Parasolid for importation into Abaqus. In Abaqus, the humeral component was simplified into an analytical rigid sphere.

3.3.1 Material properties

The components of the implant were assigned isotropic materials with a linear and elastic behavior. Their mechanical properties were defined according with the materials specified in the DePuy surgical technique catalog—the glenoid component, bone cement, and humeral head are composed of UHMWPE, Poly(methyl methacrylate) (PMMA), a cobalt-chromium alloy, respectively [53]. The mechanical properties considered are summarized in Table 3.3. Because the humeral head was modeled as a rigid analytical surface, no material properties needed to be defined.

Table 3.3: Material properties for the glenoid implant and the bone cement [53].

Material	*Young's modulus*	*Poisson's ratio*
UHMWPE	500 MPa	0.4
PMMA	2000 MPa	0.23

The properties of the scapula, however, depend on bone density. Considering a Poisson's ratio of 0.3 for bone, the Young's modulus was defined using the relationship between elasticity and bone density proposed by Gupta et. al. [64], given by:

$$E = 1049.5 \times 10^{-6}\rho^2, \ \ \rho \leq 350\ kg.m^3 \tag{3.4}$$

$$E = 3 \times 10^{-6}\rho^3, \ \ 350 < \rho \leq 1800\ kg.m^3 \tag{3.5}$$

where ρ is bone apparent density. Since the data provided by the research group also included bone densities for the scapula, estimated from the CT data using a relationship between Hounsfield units and bone density, a mapping procedure developed by the research group was applied to map the bone densities from the original geometry to the meshes of the TSA configurations. At the external surface of

the scapula, all nodes were assigned maximum bone density, $1.86 g/cm^3$. Figure 3.12 illustrates the bone density of the scapula after the application of the mapping procedure.

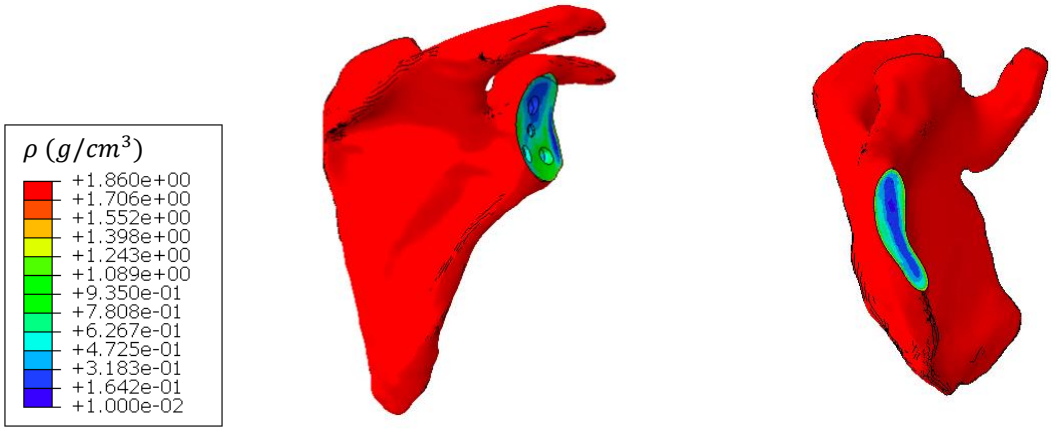

Figure 3.12: Bone density mapping for the scapula (middle) and the cut view of the scapula (right) and scale (left).

3.3.2 Mesh

The FE meshes were created individually for each component. For both the cement and glenoid component, excluding the central peg, linear hexahedral (C3D8) elements were used. The scapula and central peg of the glenoid component were meshed using quadratic tetrahedral (C3D10) elements due to their complex geometries that made impossible the generation of hexahedral elements. The size of the elements to be used was defined after a convergence analysis on the maximum contact pressure of different interfaces. The element size was settled according to convergence of results and time of simulation.

The average element size selected for the bone cement and glenoid component was 0.5mm. The resulting meshes are presented in Figure 3.13.

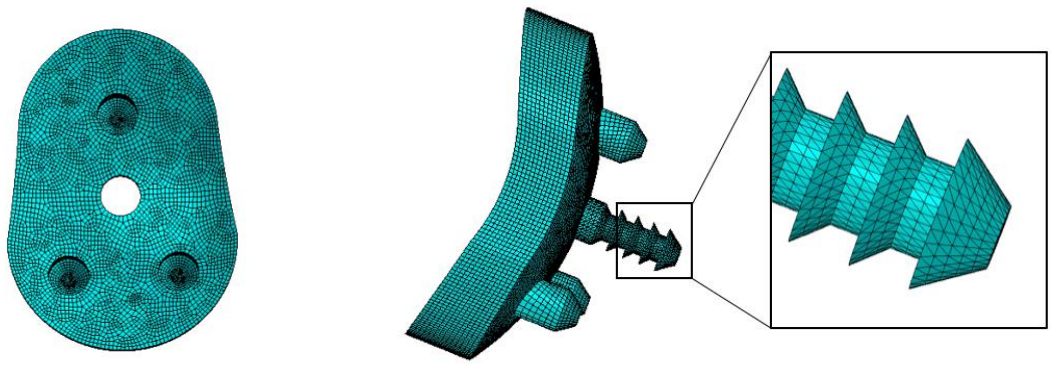

(a) (b)

Figure 3.13: Mesh of the cement (a) and the glenoid (b).

For the sake of computational simplicity, the scapula's mesh was divided into two sections, each with its own element size: the section surrounding the glenoid cavity, shown in black in Figure 3.13 (a), was assigned 1mm elements due to its expected relevance in the analysis of the failure mechanisms of glenoid loosening, while the purple area, more medialized, was assigned 2mm elements. A brief summary of the meshes properties is provided in Table 3.4.

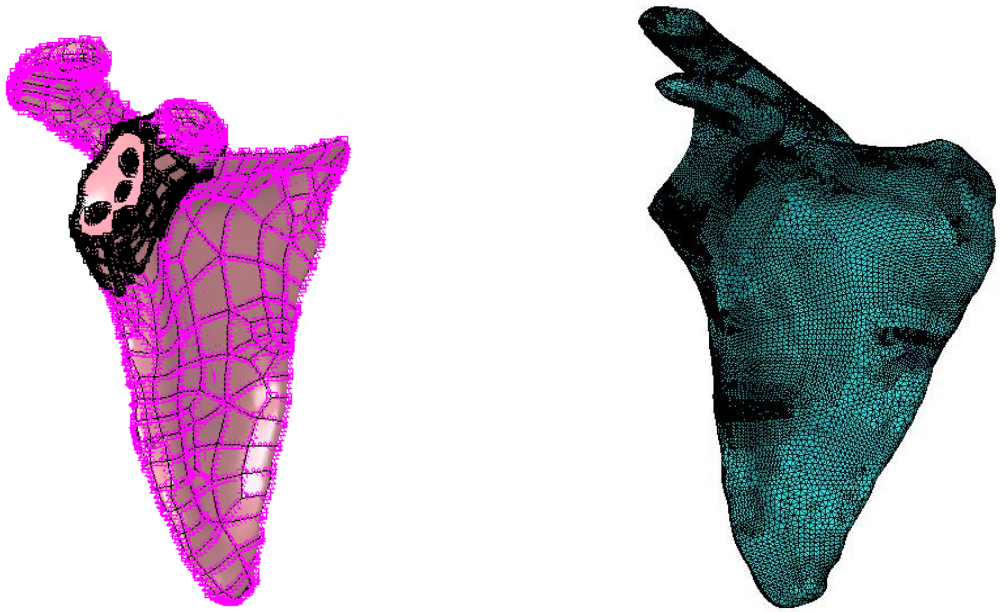

(a) (b)

Figure 3.14: Element size assignment for the scapula mesh (a) and final scapula mesh (b).

Table 3.4: Mesh summary for all components.

Part	Element type	Average element size	Number of elements	Number of nodes
Bone cement	C3D8	0.5mm	12632	18891
Glenoid component	C3D8	0.5mm	68204	75081
Glenoid central peg	C3D10	0.5mm	15077	23061
Scapula	C3D10	1mm and 2mm	349578	520678
Total assembly	-	-	445491	637679

3.3.3 Contact and interaction properties

The interactions bone-cement and cement-implant were bonded using tie constraints [59]. The interaction between the humeral head and glenoid component was modeled using a surface-to-surface contact formulation with a friction coefficient of 0.07 [59]. An automatic stabilization with a factor of 0.1 was also used to ensure model convergence. For all simulations, the static dissipation energy of the model was confirmed to be less than 5% of the total strain energy of the model, as recommended by Abaqus.

3.3.4 Loading conditions

The loading conditions applied included GH joint reaction forces for abduction and flexion movements. The loads were applied on a reference point (RP) located at the center of the humeral head, as depicted in Figure 3.15.

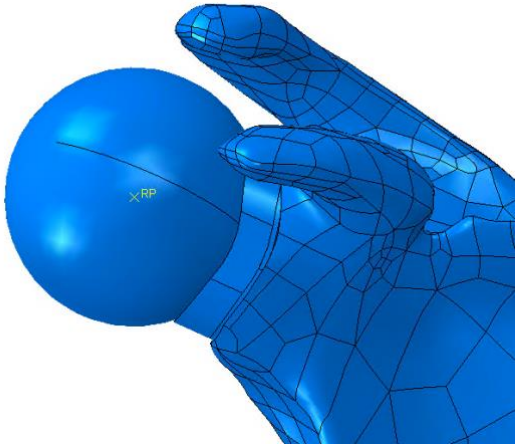

Figure 3.15: Reference point for load application on the humeral head center.

The loading conditions applied in the FE analysis included the joint reaction forces estimated by the musculoskeletal model for selected frames of abduction and flexion motions. The frames selected took into consideration the eccentricity of the loads given its relevance to the rocking-horse phenomenon and subsequent potential for implant failure [54]. Besides, the model was also used to acquire the humeral translation during the movements, which were later analyzed.

Overall, six load conditions were applied to each of the different TSA models. For the abduction movement, elevation angles of 30º, 70º and 110º were considered, while for the flexion movements, elevation angles of 30º, 80º and 105º were included. The reaction forces retrieved from the musculoskeletal model of the upper limb and applied in the FE analysis are featured in Table 3.5. These

data include the direction of the GH force, described in the scapular coordinate system [65], and the magnitude of the forces for each GH mismatch.

Table 3.5: Magnitude and direction of the load cases used in this analysis.

			Abduction			Flexion		
			30	70	110	30	80	105
1mm	Magnitude [N]		283.47	664.15	546.31	284.88	544.31	517.39
	Direction	x	-0.8601	-0.8901	-0.9233	-0.8568	-0.9247	-0.9494
		y	0.4589	0.3324	0.4897	0.4897	0.3717	0.2929
		z	-0.2225	-0.3119	-0.1615	-0.1615	-0.0826	-0.1133
3mm	Magnitude [N]		286.66	644.99	545.55	276.42	538.59	509.97
	Direction	x	-0.8572	-0.8890	-0.9284	-0.8436	-0.9167	-0.9463
		y	0.4673	0.3394	0.1704	0.5150	0.3931	0.3045
		z	-0.2161	-0.3072	-0.3303	-0.1521	-0.0718	-0.1086
5mm	Magnitude [N]		279.78	635.68	547.43	271.14	535.65	504.68
	Direction	x	-0.8532	-0.8881	-0.9310	-0.8398	-0.9050	-0.9399
		y	0.4789	0.3454	0.1728	0.5218	0.4206	0.3257
		z	-0.2067	-0.3033	-0.3216	-0.1501	-0.0629	-0.1022

3.3.5 Boundary Conditions

To complete the FE model, a boundary condition was defined to eliminate rigid body motion. To fix the scapula, an encastre condition was defined at the rhomboid muscle insertion [8], as shown in Figure 3.16.

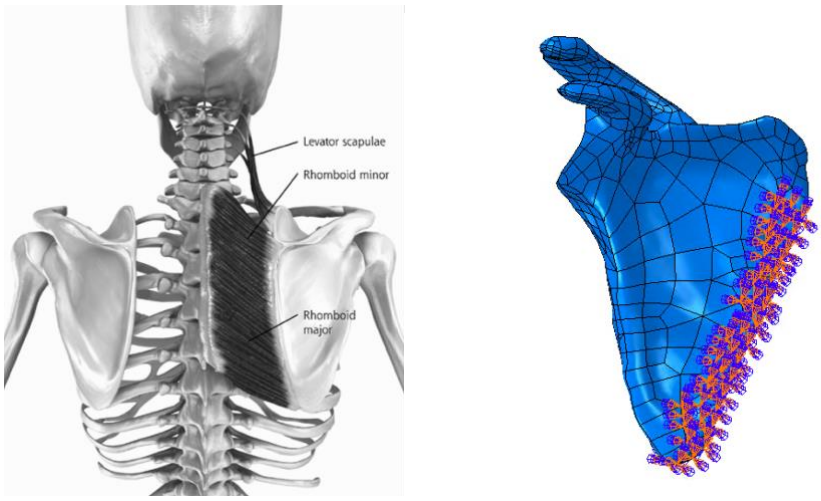

Figure 3.16: Rhomboid insertion in the scapula [9] *and respective boundary condition.*

3.4 Analysis of FE results

The processing of the data retrieved from the FE analyses was done with the goal of understanding the influence of GH conformity on the glenoid loosening mechanisms. The data gathered included Von Mises stresses for all nodes of the cement mantle and normal and shear stresses for all nodes of the bone-cement interface, which is considered the main area of glenoid loosening [8]. The Von Mises stresses in the bone cement were used to assess possible cement failure through fracture or crack generation, and the normal and shear stresses at the bone-cement interface were used to compute the Hoffman failure criterion and determine the risk of failure of the interface.

3.4.1 Evaluation of the cement stresses

The Von Mises stresses of the cement mantle were retrieved for all nodes of the cement in all loading scenarios. These values were processed and the maximum value for each node was recorded. According to the literature, PMMA failure and crack initiation starts at 5 MPa [56]. Therefore, the stresses were compared to the failure stress of the cement in order to understand the percentage of nodes at risk of cement failure.

3.4.2 Hoffman Criterion

The Hoffman criterion is a quadratic formulation that evaluates the fixation of the interface between two components. This criterion uses both normal (σ_n) and shear stresses (τ) at the interface to determine if mechanical failure may occur, by assigning to each node an Hoffman number (H) that quantifies the risk of failure of that node. According to the criterion, if H is higher than 1, failure is expected to occur, whereas if H is lower than 1, no failure is expected. The Hoffman number is determined by [64]:

$$H = \frac{1}{S_t S_c}\sigma_n^2 + \left(\frac{1}{S_t} - \frac{1}{S_c}\right)\sigma_n + \frac{1}{S_s^2}\tau^2 \tag{3.6}$$

$$S_t = 14.5\rho^{1.71} \tag{3.7}$$

$$S_c = 32.4\rho^{1.85} \tag{3.8}$$

$$S_s = 21.6\rho^{1.65} \tag{3.9}$$

where S_t and S_c are the uniaxial interface tensile and compressive strengths, respectively, and S_s is the interface shear strength. The interface strengths depend on the bone density ρ of each node.

This formulation was applied to all bone nodes from the bone-cement interface, for all load cases and different TSA configurations. To represent the worst possible scenario for each node, the highest Hoffman number among those calculated for the different load cases was selected for each node.

Chapter 4

Results

In this chapter the results from both multibody and FE analyses for all three configurations and loading cases are presented. Comparisons between the different cases are established together with quantitative and qualitative descriptions of the results.

4.1 GH joint translations after TSA

Figure 4.1 presents the reaction forces for abduction and flexion movements for the three different radial mismatches studied here. These figures allow comparing not only the magnitude of the forces to which the shoulder is subjected in different daily movements, but also its variation with the articular conformity. The magnitude of the reaction forces in both abduction and flexion increases rapidly and peaks at approximately 80º of elevation, with force magnitudes of 685N and 544N, respectively for 1mm mismatch. The GH joint reaction forces estimated during abduction were larger than those estimated during flexion.

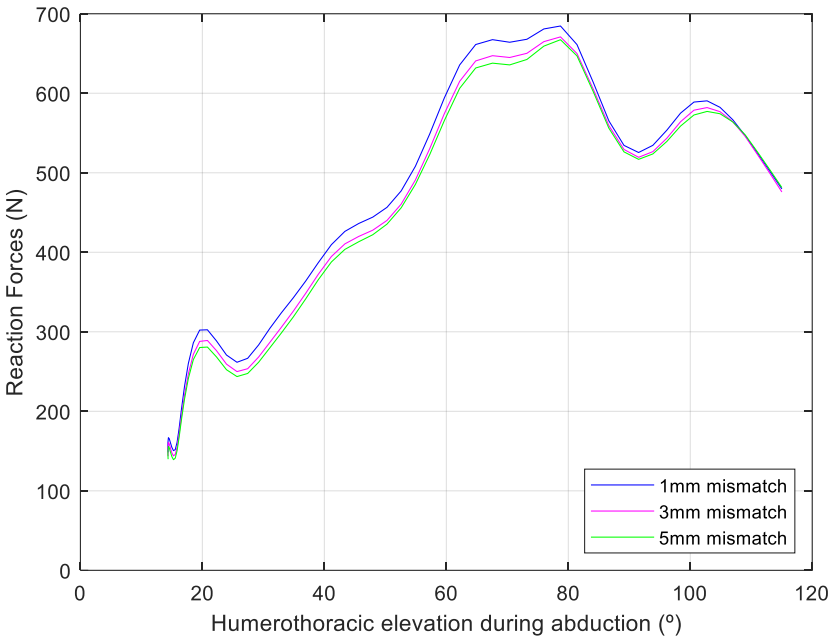

(a)

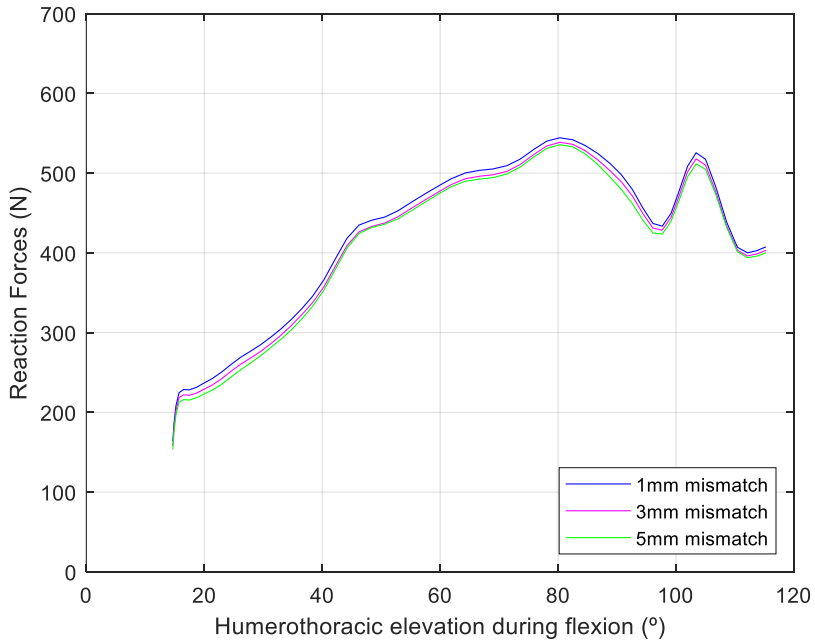

(b)

Figure 4.1:Glenohumeral reaction forces during (a) abduction and (b) flexion for radial mismatches of 1mm, 3mm and 5mm.

Figure 4.2 shows the humeral head translations over the glenoid surface during abduction and flexion movements—an increasing radial mismatch allows for wider translations of the humeral head. These

four figures allowed for the selection of which instants to analyze in the FE models. For the abduction movement, the three positions chosen corresponded to 30º, 70º and 110º of humeral elevation, while for the flexion movement, the positions selected corresponded to 30º, 80º and 105º of humeral elevation.

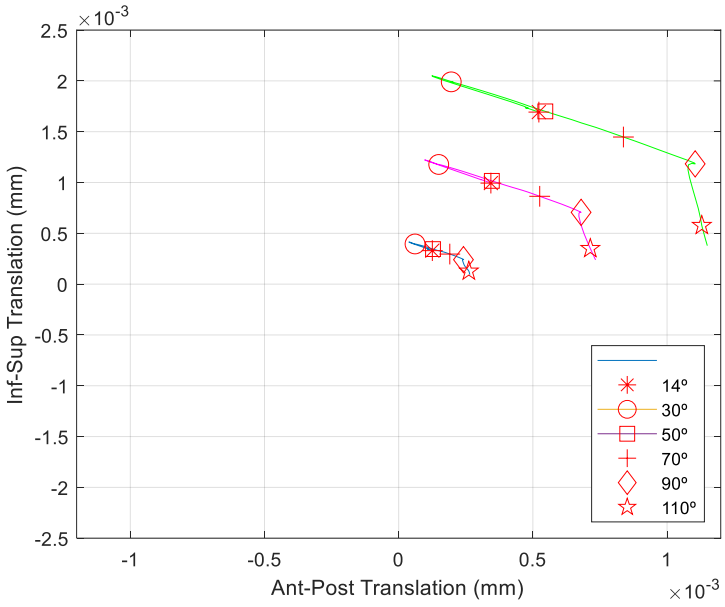

(a)

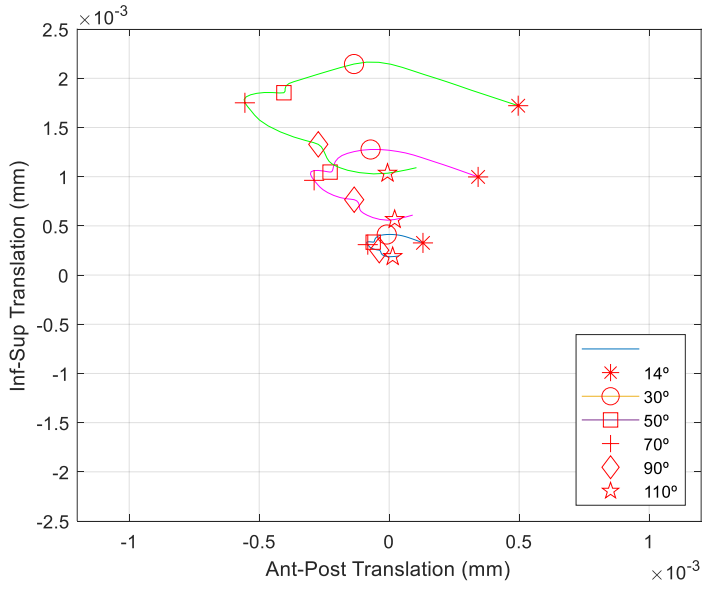

(b)

Figure 4.2:Humeral translations over the glenoid during (a) abduction and (b) flexion. Positive ant-post translations correspond to anteriorly directed translations. Positive inf-sup translations correspond to superiorly directed translations. The markers on the lines correspond to the translations on specific frames of abduction and flexion, including, 14º, 30º, 50º, 70º, 90º and 110º of humeral elevation.

4.2 Finite Element Analysis

Figure 4.3 represents the contact pressures on the PE glenoid component for the different loading cases and three conformity configurations for the abduction movement. For the sake of briefness, the results for the flexion movement are shown in Appendix I.

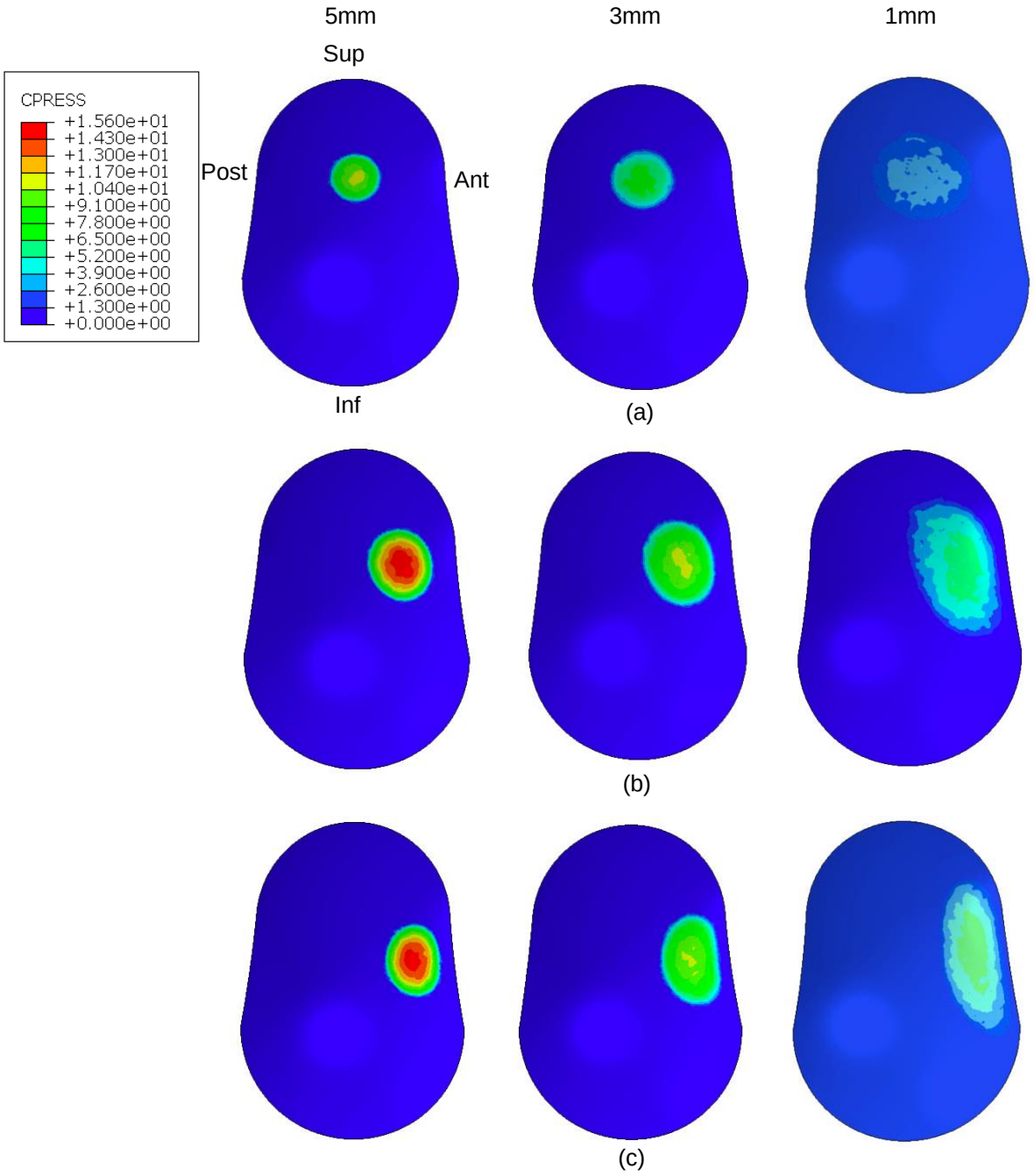

Figure 4.3: Contact pressures on the glenoid surface during abduction: (a) 30º of abduction; (b) 70º of abduction and (c) 110º of abduction. The color scale presented is applicable to all figures.

The contact area between the glenoid and humeral components decreases with increasing radial mismatch, which results in higher contact pressures in less conforming configurations.

Here on after, this section is divided into two parts that analyze the stress distributions on the cement mantle and the bone-cement interface using the Hoffman failure criterion.

4.3 Analysis of the cement mantle stresses

The 1mm thick cement mantle is placed between the glenoid implant and bone. Its stresses are a result of the propagation of stresses through the glenoid surface. The Von Mises stress distribution on the cement is depicted in Figure 4.4 and Figure 4.5 for all configurations and load cases of both abduction and flexion movements, respectively. All scales are limited to 5 MPa for easier visualization of potential fatigue failure [66]. The regions in gray correspond to those where failure might occur during cyclic loading.

All simulations presented regions surpassing the 5 MPa threshold that indicates potential failure. The region with the highest risk of failure during abduction was the most anterior area, while during flexion it was the central area and the one surrounding the superior pin of the glenoid implant. The distribution of stresses was sensitive to the articular conformity and loading conditions.

From here forward, the results show, for each radial mismatch configuration, a combination of both abduction and flexion movements and all loading cases to display the worst possible scenario, and that closest to reality since different movements are performed every day. Considering that different movements imperil different regions of the cement, for each node only the highest Von Mises stress was considered amongst all loading conditions.

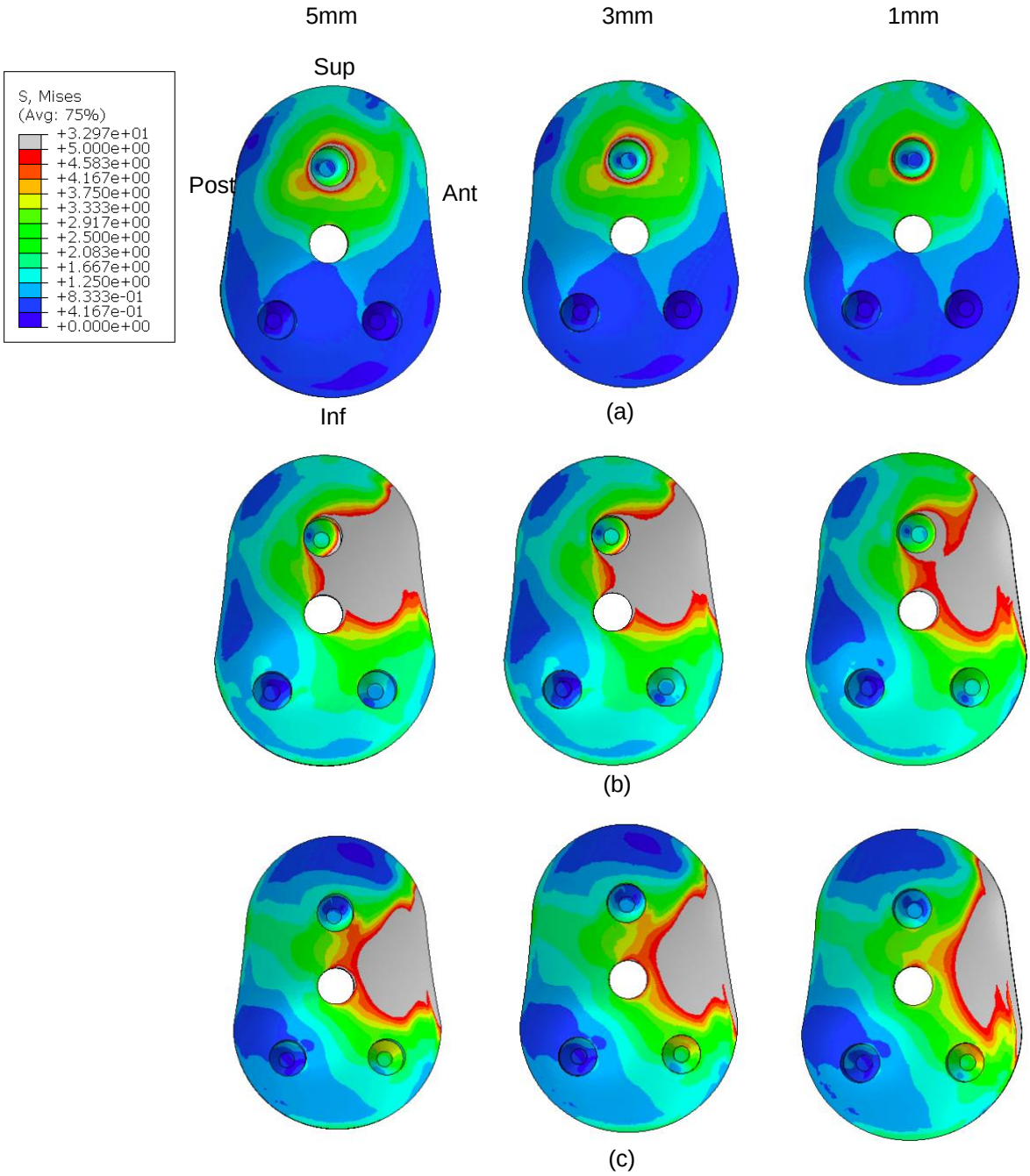

Figure 4.4: Von Mises stress distributions on the surface of the cement mantle for the three mismatches and the three load cases during abduction: (a) 30º abduction; (b) 70º abduction; (c) 110º abduction. The color scale presented is applicable to all figures.

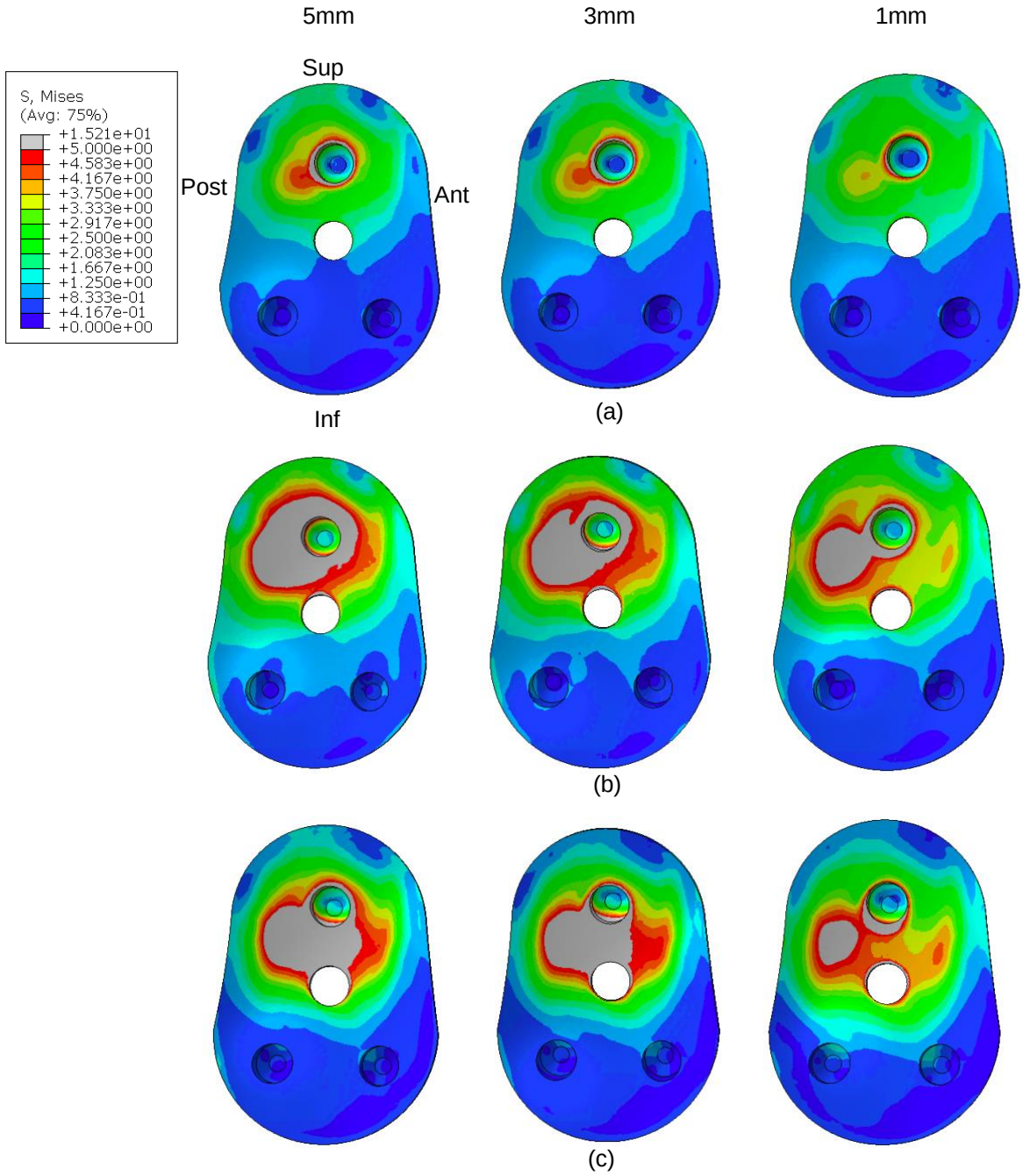

Figure 4.5: Von Mises stress distributions on the surface of the cement mantle for the three mismatches and the three load cases during flexion: (a) 30º flexion; (b) 80º flexion; (c) 105º flexion. The color scale presented is applicable to all figures.

Figure 4.6 presents the cumulative percentage of nodes that are subjected to a specific or higher Von Mises stress, for each of the three articular configurations. The vertical red line corresponds to the stress over which fatigue failure of the PMMA can occur (5 MPa [66]). In the 1mm radial mismatch configuration, the percentage of elements at risk is lower than that of other configurations. The most conforming implant resulted in a percentage of cement at risk of 23%, which increased to 27% and 28% with increasing radial mismatch. However, at higher levels of stress, from 5 MPa to 10 MPa the

difference between radial mismatches is larger. At 7MPa, the percentages at risk for 1mm, 3mm and 5mm were 7%, 15% and 16% respectively.

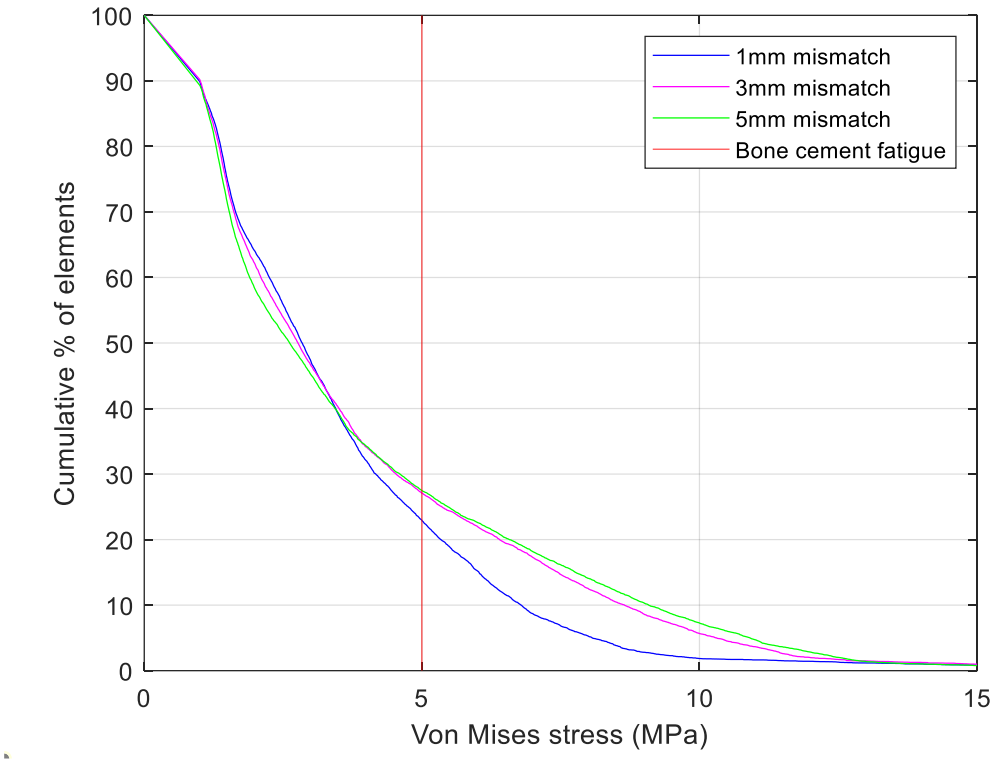

Figure 4.6: Cumulative percentage of nodes that are under a specific Von Mises stress or higher.

4.4 Hoffman failure criterion

The distribution of the Hoffman numbers along the surface of the scapula connected to the PMMA is depicted in Figure 4.7 for the three configurations under study. According to the Hoffman criterion, regions above 1 are at risk of debonding. Therefore, to make the analysis easier, the Hoffman numbers are presented between 0 and 1—the regions where failure of the interface might occur are shown in gray.

The anterior region presented an Hoffman number higher than 1 regardless of the conformity of the joint. As the radial mismatch increased, the Hoffman number also increased on the region of the upper peg. For the largest radial mismatch, the superior peg presents Hoffman numbers larger than 1, which was not observed for the remaining configurations. The areas in black correspond to negative Hoffman numbers.

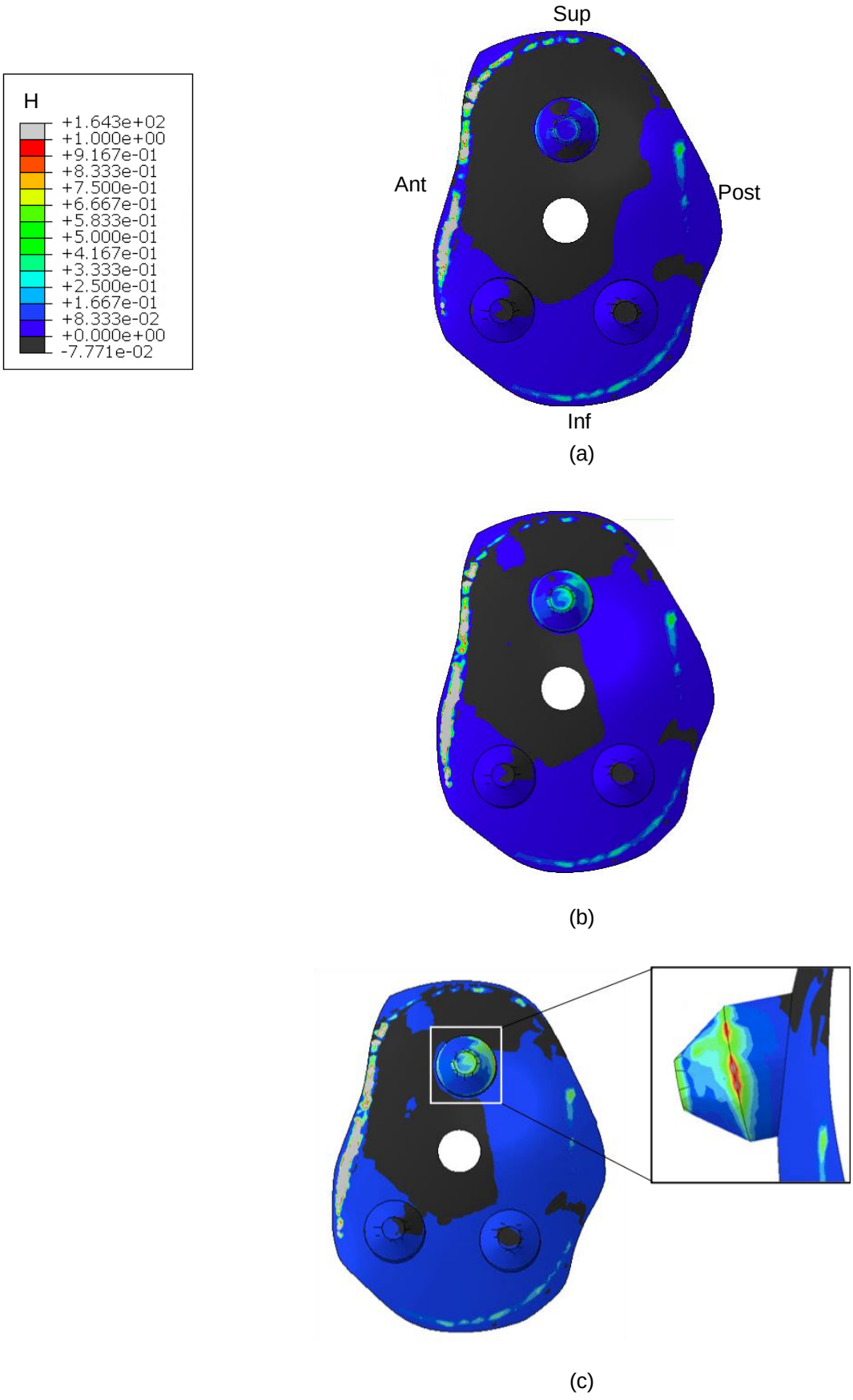

Figure 4.7: Hoffman number distributions for (a) 1mm mismatch; (b) 3mm mismatch and (c) 5mm mismatch. The orientation of the images is depicted in (a). The color scale presented is applicable to all figures.

Figure 4.8 presents the percentage of nodes of the bone-cement interface that are above a certain Hoffman number, between 0 and 1, for the different conformities. The cumulative percentage of nodes with Hoffman number above zero does not start at 100% because some of the Hoffman numbers were negative, and, for the ease of the analyses, these numbers were neglected from the plot. The results show that most nodes had low Hoffman numbers, and that for high Hoffman numbers the difference between radial mismatches seemed negligible.

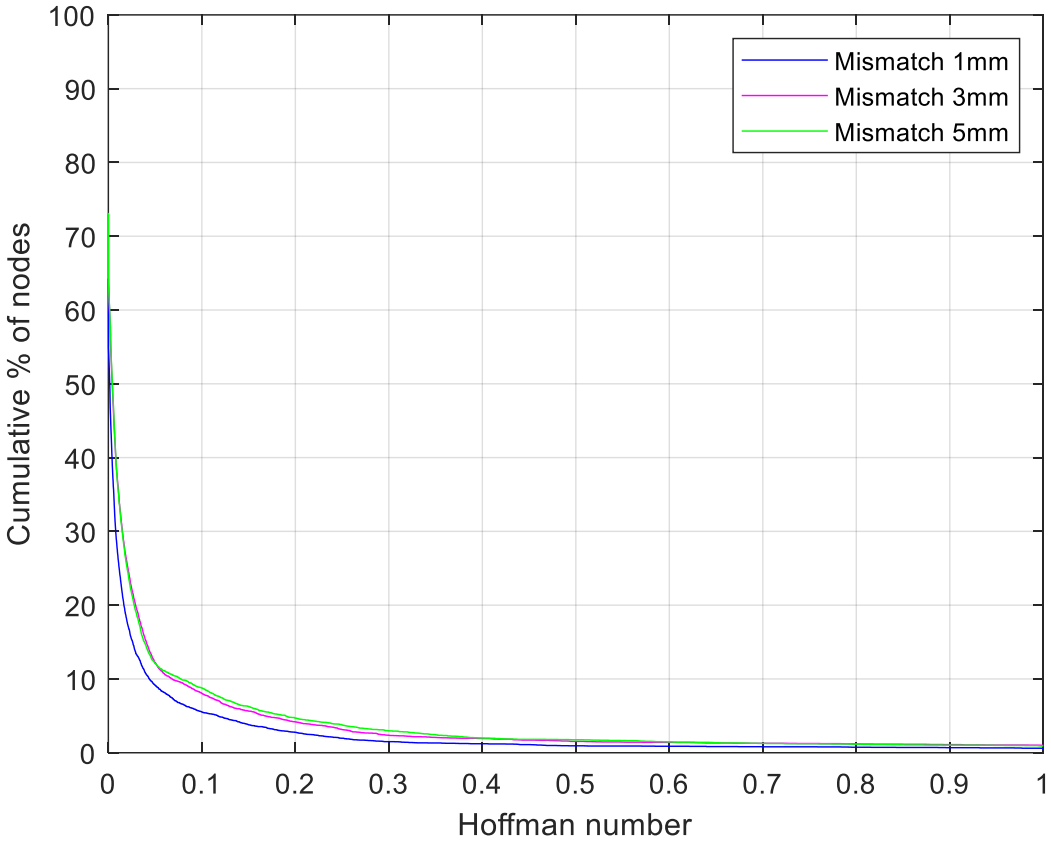

Figure 4.8: Cumulative percentage of nodes with Hoffman number between 0 and 1.

Chapter 5

Discussion

This study aimed to evaluate the influence of the articular conformity in the mechanisms of glenoid loosening after an anatomic TSA. The three configurations analyzed had radial mismatches of 1mm, 3mm and 5mm and were subjected to six loading conditions each (abduction and flexion movements in three arm positions), which were obtained through the application of a musculoskeletal model of the upper limb [60].

Regarding the joint reaction forces at the GH joint, no relevant differences were observed in the magnitudes between different radial mismatches, even though the force increased with joint conformity. These results are consistent with previous computational models, which observed no influence of the GH translations on the joint reaction forces [60].

The humeral translations estimated by the musculoskeletal model increased with decreasing conformity, which is consistent with the less restricted kinematics of the joint (Figure 4.2). These results are supported by the literature. In fact, Hopkins et. al. [67] conducted a 3D FE analysis and have shown that under conditions of simple compressive loading, the humeral translations depended linearly on glenohumeral conformity, the most conforming the joint, the least humeral translations were allowed.

Moreover, the increasing mismatch also resulted in a decrease in contact area between the humeral head and glenoid components, and thus in an increase in contact pressure (Figure 4.3). Once again, the results are consistent with previous studies that show that not only decreased conformity leads to smaller contact areas, but also that the contact area has critical influence on the stress levels. Studies have found that for small contact areas the contact stresses increase, as found in the present study [4], [68].

The mechanisms of glenoid loosening were analyzed through the potential failure of the PMMA and the bone-cement interface. The evaluation of Von Mises stresses in the bone cement suggested that

glenoid loosening may be a result of fatigue failure of the PMMA in all configurations, with emphasis on less conforming designs, as a high percentage of the cement was under stresses higher than 5 MPa, considered to be the fatigue strength of the PMMA [56]. At 7MPa, the percentage of nodes at risk in low-conforming configurations was twice that of the most conforming configuration. This is consistent with the literature—Lacroix and Prendergast [56] found similar results for a keeled implant, concluding that more conforming designs lead to more moderate stresses on the cement mantle. Moreover, Terrier et. al. [69] have shown that the Von Mises stress increased around 200% as the mismatch increased from 1 to 15mm, which is in line with the increasing stress on the cement mantle for increasing mismatch seen in this study.

Additionally, note that this study considered loading cases of unloaded abduction and flexion movements. Under other daily activities, the cement mantle may be subjected to much higher stresses, supporting the concern of cement failure.

Moreover, the value for the cement fatigue strength is not clear in the literature, ranging from 4MPa to 15 MPa, depending on the number of cycles and on the study performed [8]. Therefore, this analysis may be different if a higher reference is taken into consideration. Nevertheless, the 5 MPa reference was chosen since it has been used in similar studies [52], [56].

The analysis of bone-cement interface using the Hoffman criterion showed that failure can occur in all configurations on the anterior region of the bone-cement interface. This zone presents low bone density (Figure 3.12), which is another important factor when evaluating glenoid loosening mechanisms. In the two most conforming configurations, the only zone of the interface that failed was the anterior boundary; however, for the highest radial mismatch, the area surrounding the superior peg was also failing according to the Hoffman criterion.

Using both criteria, glenoid loosening may begin through cement failure and bone-cement debonding. Besides, the probability of cement failure of high-conformity joints is lower than that of low articular conformity designs. Moreover, according to the Hoffman criterion, the largest mismatch presents two different areas of possible detachment and therefore is believed to be worse performing than the other designs.

To sum up, for all radial mismatches studied, the configuration with highest conformity showed the lowest risk of failure, while the other two configurations showed similar results, with a difference in the evaluation of bone-cement detachment, where the 5mm mismatch design performed worse.

The findings of this study must be evaluated considering its limitations. Firstly, the loading scenarios were limited since a wide range of movements are performed every day. Daily living activities may be better suited for identifying different failure mechanisms of glenoid loosening. Secondly, the analysis was performed considering one specific shoulder joint anatomy, thus, the results may not be generalized for all glenohumeral joint.

Moreover, the evaluation of the distribution of stresses on the cement mantle considered the fatigue strength of the material and crack generation under cyclic loading, even though only static analyses

were performed in this study. Besides, as mentioned before, there is no consensus in the literature regarding the failure strength of the cement.

The bone-cement and cement-implant interactions were assumed bonded, which does not allow for micromotion evaluation, as analyzed in some studies [53]. The evaluation of the micromotions would allow for the analysis of the implant-cement interface. Even though this is not considered to be the most relevant interface when studying glenoid loosening mechanisms, it would be interesting to evaluate and confirm whether the radial mismatch influences the interface failure.

Finally, the influence of bone density in all the evaluation criteria may have conditioned the results since a low-density region existed in the superior region of the reamed glenoid cavity.

Chapter 6

Conclusions and future work

6.1 Conclusions

This study performed 3D FE analyses of three articular configurations after TSA, for radial mismatches of 1mm, 3mm and 5mm, which allowed for the evaluation of the influence of the GH conformity in the failure mechanisms of the glenoid implant. Translations of the humeral head along the glenoid were evaluated and both cement failure and bone-cement interface detachment were analyzed through stress distribution on the cement and the Hoffman failure criterion, respectively.

The translations of the humeral head retrieved from the multibody model have shown that larger radial mismatches allow for greater humeral translations.

The stress distribution of the cement showed that fatigue failure and crack initiation is in the spectrum of possible complications since in all configurations stresses surpassed the endurance limit of the PMMA. For a 1mm radial mismatch, the percentage of nodes at risk was 7%, while for the 3mm and 5mm mismatches, this percentage doubled.

The Hoffman criterion analysis suggested two zones of possible detachment between the cement and bone, namely the superior peg and the regions with low bone density. Overall, the results suggested that the most conforming configuration has lower risks of failure under normal and healthy physiological conditions when compared to less conforming designs. However, this configuration is still at risk of failure through both mechanisms identified.

Despite glenoid loosening being the most common complication of anatomic TSA, the influence of its design features on the stability of the joint is not yet fully understood. As very few general studies analyze the influence of glenohumeral conformity in joint stability, and currently no FE analyses of different glenoid conformities for anatomical TSA under physiological conditions exist, this study sought to expand the knowledge and understanding of the articular conformity on the failure mechanisms of the glenoid.

6.2 Future work

The future work to be developed on this topic involves surpassing the limitations of the current study.

Therefore, to analyze the influence of this design parameter on other glenoid loosening mechanisms, lesion of the rotator cuff muscles may be simulated, since it is believed to be the principal trigger of the rocking-horse phenomenon.

Excluding the contact between the humeral head and glenoid components, all interactions were defined as bonded using tie constraints. It would be interesting to also consider these interactions as contacting surfaces with friction [53]. This would allow the application of other criteria: for example, the evaluation of possible glenoid micromotions and displacements away from the cement.

Finally, in this study, the loading conditions were only retrieved from two types of movement: abduction and flexion. In order to have a more comprehensive loading scenario, a broader range of movements should be analyzed (at the cost of computational complexity) since other failure mechanisms can be better identified during other movements.

References

[1] E. P. Occhiboi and R. D. Clement, “Anatomic Total Shoulder Arthroplasty and Reverse Total Shoulder Arthroplasty,” *JBJS J. Orthop. Physician Assist.*, vol. 8, no. 1, p. 0025, 2020, doi: 10.2106/JBJS.JOPA.19.00025.

[2] T. M. Gregory, B. Boukebous, J. Gregory, J. Pierrart, and E. Masemjean, “Suppl-6, M6: Short, Medium and Long Term Complications After Total Anatomical Shoulder Arthroplasty,” *Open Orthop. J.*, vol. 11, no. 1, p. 1133, Oct. 2017, doi: 10.2174/1874325001711011133.

[3] J. L. Franklin, W. P. Barrett, S. E. Jackins, and -I-and A Frederick Matsen HI, “Glenoid Loosening in Total Shoulder Arthroplasty Association With Rotator Cuff Deficiency.”

[4] G. Walch, T. Bradley Edwards, A. Boulahia, P. Boileau, D. Mole, and P. Adeleine, “The influence of glenohumeral prosthetic mismatch on glenoid radiolucent lines: results of a multicenter study,” *J. Bone Joint Surg. Am.*, vol. 84, no. 12, pp. 2186–2191, Dec. 2002, doi: 10.2106/00004623-200212000-00010.

[5] C. Anglin, U. P. Wyss, R. W. Nyffeler, and C. Gerber, “Loosening performance of cemented glenoid prosthesis design pairs,” *Clin. Biomech.*, vol. 16, no. 2, pp. 144–150, Feb. 2001, doi: 10.1016/S0268-0033(00)00078-4.

[6] B. Couteau, P. Mansat, E. Estivalèzes, R. Darmana, M. Mansat, and J. Egan, “Finite element analysis of the mechanical behavior of a scapula implanted with a glenoid prosthesis,” *Clin. Biomech.*, vol. 16, no. 7, pp. 566–575, Aug. 2001, doi: 10.1016/S0268-0033(01)00029-8.

[7] V. J. Sabesan, J. Ackerman, V. Sharma, K. C. Baker, M. D. Kurdziel, and J. M. Wiater, “Glenohumeral mismatch affects micromotion of cemented glenoid components in total shoulder arthroplasty,” *J. Shoulder Elb. Surg.*, vol. 24, no. 5, pp. 814–822, May 2015, doi: 10.1016/J.JSE.2014.10.004.

[8] A. Terrier, P. Büchler, and A. Farron, “Bone-cement interface of the glenoid component: stress analysis for varying cement thickness,” *Clin. Biomech. (Bristol, Avon)*, vol. 20, no. 7, pp. 710–717, Aug. 2005, doi: 10.1016/J.CLINBIOMECH.2005.03.010.

[9] T. Dimon Jr, “Anatomy of the Moving Body A Basic Course in Bones, Muscles, and Joints.” p. 272, 2008.

[10] F. Matter, *Anatomy & Phisiology: The Unity of Form and Function*, Third. 2003.

[11] E. Mostafa, O. Imonugo, and M. Varacallo, “Anatomy, Shoulder and Upper Limb, Humerus,” *StatPearls*, Aug. 2021, Accessed: Oct. 29, 2021. [Online]. Available: https://www.ncbi.nlm.nih.gov/books/NBK534821/.

[12] M. Mancuso, “Evaluation and robotic simulation of the glenohumeral joint.,” 2020.

[13] “Standard (Anatomic) Total Shoulder Replacement | Dr. Gordon Groh.” https://www.drgordongroh.com/orthopaedic-injuries-treatment/shoulder/standard-total-shoulder-replacement/ (accessed Sep. 07, 2021).

[14] C. S. Neer, “The classic: Articular replacement for the humeral head. 1955,” *Clin. Orthop. Relat. Res.*, vol. 469, no. 9, pp. 2409–2421, 2011, doi: 10.1007/S11999-011-1944-5.

[15] Maslow Jed ; Wanner John Paul; Routman Howard ; Byram Ian, “The Disappearing Stem: The Changing Humeral Side of Shoulder Arthroplasty | International Congress for Joint Reconstruction,” Accessed: Oct. 21, 2021. [Online]. Available: https://icjr.net/articles/the-disappearing-stem-the-changing-humeral-side-of-shoulder-arthroplasty.

[16] DePuy Synthes, “Global AP Surgical technique.”

[17] “AEQUALIS ASCEND ™ FLEX Convertible Shoulder System.”

[18] “SIMPLICITI™ Shoulder System - Wright Medical Group.” https://www.wright.com/products-upper/simpliciti-shoulder-arthroplasty-system (accessed Oct. 22, 2021).

[19] C. S. Neer, “Replacement arthroplasty for glenohumeral osteoarthritis,” *J. Bone Joint Surg. Am.*, vol. 56, no. 1, pp. 1–13, 1974, Accessed: Sep. 08, 2021. [Online]. Available: https://pubmed.ncbi.nlm.nih.gov/4812164/.

[20] C. S. Neer, K. C. Watson, and F. Stanton, “Recent experience in total shoulder replacement,” *J. Bone Joint Surg. Am.*, vol. 64, no. 3, pp. 327–329, Jan. 1982, Accessed: Sep. 08, 2021. [Online]. Available: https://pubmed.ncbi.nlm.nih.gov/7061549/.

[21] A. Castagna and R. Garofalo, “Journey of the glenoid in anatomic total shoulder replacement,” doi: 10.1177/1758573218790119.

[22] Tornier, “AEQUALIS ™ PERFORM Anatomic Glenoid System ™.”

[23] Lima Corporate, “SMR AXIOMA TT METAL BACK,” Accessed: Oct. 27, 2021. [Online]. Available: www.limacorporate.com.

[24] R. S. Churchill, R. S. Boorman, E. V Fehringer, and F. A. Matsen, “Glenoid cementing may generate sufficient heat to endanger the surrounding bone,” *Clin. Orthop. Relat. Res.*, no. 419, pp. 76–79, 2004, doi: 10.1097/00003086-200402000-00013.

[25] M. J. Taunton, A. L. Mcintosh, J. W. Sperling, and R. H. Cofield, “Total Shoulder Arthroplasty with a Metal-Backed, Bone-Ingrowth Glenoid Component Medium to Long-Term Results,” doi: 10.2106/JBJS.G.00966.

[26] DePuy Synthes, “GLOBAL™ APG Anchor Peg Glenoid Shoulder System Surgical Technique.”

[27] Depuy, “anchor PEG GLENOID - DESIGN RATIONALE AND SURGICAL TECHNIQUE.”

[28] F. A. Matsen and C. Rockwood, “Anatomic shoulder arthroplasty.”

[29] K. I. Bohsali, B. Aaron J, and W. Michael A, “Complications of Shoulder Arthroplasty,” *Copyr. Ó 2017 BY J. BONE Jt. Surg.*, vol. 99, pp. 256–69, 2017, doi: 10.2106/JBJS.16.00935.

[30] L. MATTEI, S. MORTERA, C. ARRIGONI, and F. CASTOLDI, “Anatomic shoulder arthroplasty: an update on indications, technique, results and complication rates,” *Joints*, vol. 3, no. 2, p. 72, Apr. 2015, doi: 10.11138/JTS/2015.3.2.072.

[31] K. I. Bohsali, M. A. Wirth, and C. A. Rockwood, “Complications of total shoulder arthroplasty,” *J. Bone Joint Surg. Am.*, vol. 88, no. 10, pp. 135–141, 2006, doi: 10.2106/JBJS.F.00125.

[32] A. K. Franta, T. R. Lenters, D. Mounce, B. Neradilek, and F. A. Matsen, “The complex characteristics of 282 unsatisfactory shoulder arthroplasties,” *J. shoulder Elb. Surg.*, vol. 16, no. 5, pp. 555–562, Sep. 2007, doi: 10.1016/J.JSE.2006.11.004.

[33] F. A. Matsen, R. T. Bicknell, and S. B. Lippitt, “Shoulder arthroplasty: the socket perspective,” *J. shoulder Elb. Surg.*, vol. 16, no. 5 Suppl, Sep. 2007, doi: 10.1016/J.JSE.2007.02.112.

[34] B. P. Buckingham, I. M. Parsons, B. Campbell, R. M. Titelman, K. L. Smith, and F. A. Matsen, “Patient functional self-assessment in late glenoid component failure at three to eleven years after total shoulder arthroplasty,” *J. shoulder Elb. Surg.*, vol. 14, no. 4, pp. 368–374, Jul. 2005, doi: 10.1016/J.JSE.2004.10.008.

[35] F. A. Matsen, J. Clinton, J. Lynch, A. Bertelsen, and M. L. Richardson, “Glenoid Component Failure in Total Shoulder Arthroplasty,” *This is an Enhanc. PDF from J. Bone Jt. Surg.*, vol. 90, pp. 885–896, 2008, doi: 10.2106/JBJS.G.01263.

[36] B. S. Schoch *et al.*, “Glenoid component lucencies are associated with poorer patient-reported outcomes following anatomic shoulder arthroplasty,” *J. Shoulder Elb. Surg.*, vol. 28, pp. 1956–1963, 2019, doi: 10.1016/j.jse.2019.03.011.

[37] P. Vavken, P. Sadoghi, A. Von Keudell, C. Rosso, V. Valderrabano, and A. M. Müller, “Rates of radiolucency and loosening after total shoulder arthroplasty with pegged or keeled glenoid components,” *J. Bone Jt. Surg. - Ser. A*, vol. 95, no. 3, pp. 215–221, Feb. 2013, doi: 10.2106/JBJS.L.00286.

[38] A. Papadonikolakis and F. A. Matsen, “Metal-backed glenoid components have a higher rate of failure and fail by different modes in comparison with all-polyethylene components: A systematic review,” *J. Bone Jt. Surg. - Am. Vol.*, vol. 96, no. 12, pp. 1041–1047, Jun. 2014, doi: 10.2106/JBJS.M.00674.

[39] S. B. Gunther, J. Graham, T. R. Norris, M. D. Ries, and L. Pruitt, “Retrieved glenoid components: A classification system for surface damage analysis,” *J. Arthroplasty*, vol. 17, no. 1, pp. 95–100, 2002, doi: 10.1054/ARTH.2002.27671.

[40] J. P. Braman, A. Falicov, R. Boorman, and F. A. Matsen, “Alterations in surface geometry in retrieved polyethylene glenoid component,” *J. Orthop. Res.*, vol. 24, no. 6, pp. 1249–1260, Jun. 2006, doi: 10.1002/JOR.20158.

[41] C. Quental, P. R. Fernandes, J. Monteiro, and J. Folgado, “Bone remodelling of the scapula after a total shoulder arthroplasty,” *Biomech. Model. Mechanobiol. 2013 134*, vol. 13, no. 4, pp. 827–838, Oct. 2013, doi: 10.1007/S10237-013-0537-5.

[42] F. Familiari, G. Huri, and E. G. Mcfarland, “Supraspinatus tears after total shoulder arthroplasty: A review of diagnosis and treatment,” *Semin. Arthroplasty*, vol. 25, pp. 64–70, 2014, doi: 10.1053/j.sart.2014.02.011.

[43] C. S. Neer, E. V Craig, H. Fukuda, and N. York, “Cuff-Tear Arthropathy.”

[44] M. Zheng, Z. Zou, P. jorge D. silva Bartolo, C. Peach, and L. Ren, “Finite element models of the human shoulder complex: a review of their clinical implications and modelling techniques,” *Int. j. numer. method. biomed. eng.*, vol. 33, no. 2, Feb. 2017, doi: 10.1002/CNM.2777.

[45] C. Högfors, D. Karlsson, and B. Peterson, “Structure and internal consistency of a shoulder model,” *J. Biomech.*, vol. 28, no. 7, pp. 767–777, 1995, doi: 10.1016/0021-9290(94)00134-P.

[46] A. Stops, R. Wilcox, and Z. Jin, “Computational modelling of the natural hip: a review of finite element and multibody simulations,” *Comput. Methods Biomech. Biomed. Engin.*, vol. 15, no. 9, pp. 963–979, Sep. 2012, doi: 10.1080/10255842.2011.567983.

[47] B. E. Rapp, “Finite Element Method,” *Microfluid. Model. Mech. Math.*, pp. 655–678, Jan. 2017, doi: 10.1016/B978-1-4557-3141-1.50032-0.

[48] R. Huiskes and S. J. Hollister, “From structure to process, from organ to cell: recent developments of FE-analysis in orthopaedic biomechanics,” *J. Biomech. Eng.*, vol. 115, no. 4B, pp. 520–527, 1993, doi: 10.1115/1.2895534.

[49] A. Terrier, A. Reist, A. Vogel, and A. Farron, “Effect of supraspinatus deficiency on humerus translation and glenohumeral contact force during abduction,” *Clin. Biomech. (Bristol, Avon)*, vol. 22, no. 6, pp. 645–651, Jul. 2007, doi: 10.1016/J.CLINBIOMECH.2007.01.015.

[50] N. Seki *et al.*, “Mechanical environment of the supraspinatus tendon: three-dimensional finite element model analysis,” *J. Orthop. Sci. 2008 134*, vol. 13, no. 4, pp. 348–353, Aug. 2008, doi: 10.1007/S00776-008-1240-8.

[51] B. J. Ellis, N. J. Drury, S. M. Moore, P. J. McMahon, J. A. Weiss, and R. E. Debski, “Finite element modelling of the glenohumeral capsule can help assess the tested region during a clinical exam,” *Comput. Methods Biomech. Biomed. Engin.*, vol. 13, no. 3, pp. 413–418, 2010, doi: 10.1080/10255840903317378.

[52] D. Lacroix, L. Murphy, and P. Prendergast, “Three-dimensional finite element analysis of glenoid replacement prostheses: a comparison of keeled and pegged anchorage systems,” *J. Biomech. Eng.*, vol. 122, no. 4, pp. 430–436, 2000, doi: 10.1115/1.1286318.

[53] W. Pomwenger, K. Entacher, H. Resch, and P. Schuller-Götzburg, “Influence of glenoid implant depth on the bone–polymethylmethacrylate interface,” *Obere Extrem. 2019 144*, vol. 14, no. 4, pp. 284–291, Mar. 2019, doi: 10.1007/S11678-019-0512-6.

[54] A. Karelse, A. Van Tongel, T. Verstraeten, D. Poncet, and L. F. De Wilde, “Rocking-horse phenomenon of the glenoid component: the importance of inclination,” *J. shoulder Elb. Surg.*, vol. 24, no. 7, pp. 1142–1148, Jul. 2015, doi: 10.1016/J.JSE.2014.12.017.

[55] A. R. Hopkins, U. N. Hansen, A. A. Amis, and R. Emery, “The effects of glenoid component alignment variations on cement mantle stresses in total shoulder arthroplasty,” *J. shoulder Elb. Surg.*, vol. 13, no. 6, pp. 668–675, Nov. 2004, doi: 10.1016/S1058274604001399.

[56] D. Lacroix and P. Prendergast, “Stress analysis of glenoid component designs for shoulder arthroplasty,” *Proc. Inst. Mech. Eng. H.*, vol. 211, no. 6, pp. 467–474, 1997, doi: 10.1243/0954411981534583.

[57] R. J. Friedman, M. Laberge, R. L. Dooley, and A. L. O’hara, “Finite element modeling of the glenoid component: Effect of design parameters on stress distribution,” doi: 10.1016/S1058-2746(09)80068-2.

[58] K. D. Stone, J. J. Grabowski, R. H. Cofield, B. F. Morrey, and K. N. An, “Stress analyses of glenoid components in total shoulder arthroplasty,” *J. shoulder Elb. Surg.*, vol. 8, no. 2, pp. 151–158, 1999, doi: 10.1016/S1058-2746(99)90009-5.

[59] J. Zhang *et al.*, “Glenoid articular conformity affects stress distributions in total shoulder arthroplasty,” *J. Shoulder Elb. Surg.*, vol. 22, no. 3, pp. 350–356, Mar. 2013, doi: 10.1016/J.JSE.2012.08.025.

[60] C. Quental, J. Folgado, J. Ambrósio, and J. Monteiro, “A new shoulder model with a biologically inspired glenohumeral joint,” *Med. Eng. Phys.*, vol. 38, no. 9, pp. 969–977, Sep. 2016, doi: 10.1016/J.MEDENGPHY.2016.06.012.

[61] Integra LifeSciences, “TITAN Modular Shoulder System,” 2013. [Online]. Available: http://integralife.com/index.aspx?redir=detailproduct&Product=735&ProductName=TITAN® Modular Shoulder System&ProductLineName=Shoulder & Elbow&ProductLineID=72&PA=Upper Extremity.

[62] V. J. Sabesan, D. J. L. Lima, J. D. Whaley, V. Pathak, and L. Zhang, “The effect of glenohumeral radial mismatch on different augmented total shoulder arthroplasty glenoid designs: a finite element analysis,” *J. shoulder Elb. Surg.*, vol. 28, no. 6, pp. 1146–1153, Jun. 2019, doi: 10.1016/J.JSE.2018.11.059.

[63] M. Machado *et al.*, “Development of a planar multibody model of the human knee joint,” *Nonlinear Dyn.*, vol. 60, no. 3, pp. 459–478, May 2010, doi: 10.1007/S11071-009-9608-7.

[64] S. Gupta, F. C. T. Van der Helm, and F. Van Keulen, “The possibilities of uncemented glenoid component--a finite element study,” *Clin. Biomech. (Bristol, Avon)*, vol. 19, no. 3, pp. 292–302, Mar. 2004, doi: 10.1016/J.CLINBIOMECH.2003.12.002.

[65] C. Quental, J. Folgado, J. Ambrósio, and J. Monteiro, “A multibody biomechanical model of the upper limb including the shoulder girdle,” *Multibody Syst. Dyn.*, vol. 28, no. 1–2, pp. 83–108, Aug. 2012, doi: 10.1007/S11044-011-9297-0.

[66] J. P. Davies, D. W. Burke, D. O. O’Connor, and W. H. Harris, “Comparison of the fatigue characteristics of centrifuged and uncentrifuged Simplex P bone cement,” *J. Orthop. Res.*, vol. 5, no. 3, pp. 366–371, 1987, doi: 10.1002/JOR.1100050308.

[67] H. Andrew R, H. Ulrich N, A. Andrew A, T. Mark, and E. Roger J, “Glenohumeral kinematics following total shoulder arthroplasty: a finite element investigation,” *J. Orthop. Res.*, vol. 25, no. 1, pp. 108–115, Jan. 2007, doi: 10.1002/JOR.20290.

[68] B. Couteau, P. Mansat, E. Estivalèzes, R. Darmana, M. Mansat, and J. Egan, “Finite element analysis of the mechanical behavior of a scapula implanted with a glenoid prosthesis,” *Clin. Biomech. (Bristol, Avon)*, vol. 16, no. 7, pp. 566–575, 2001, doi: 10.1016/S0268-0033(01)00029-8.

[69] A. Terrier, P. Büchler, and A. Farron, “Influence of glenohumeral conformity on glenoid stresses after total shoulder arthroplasty,” 2006, doi: 10.1016/j.jse.2005.09.021.

Appendix A

In Fig XX the results for the contact pressures during flexion are presented for all mismatches studied and for all loading conditions.

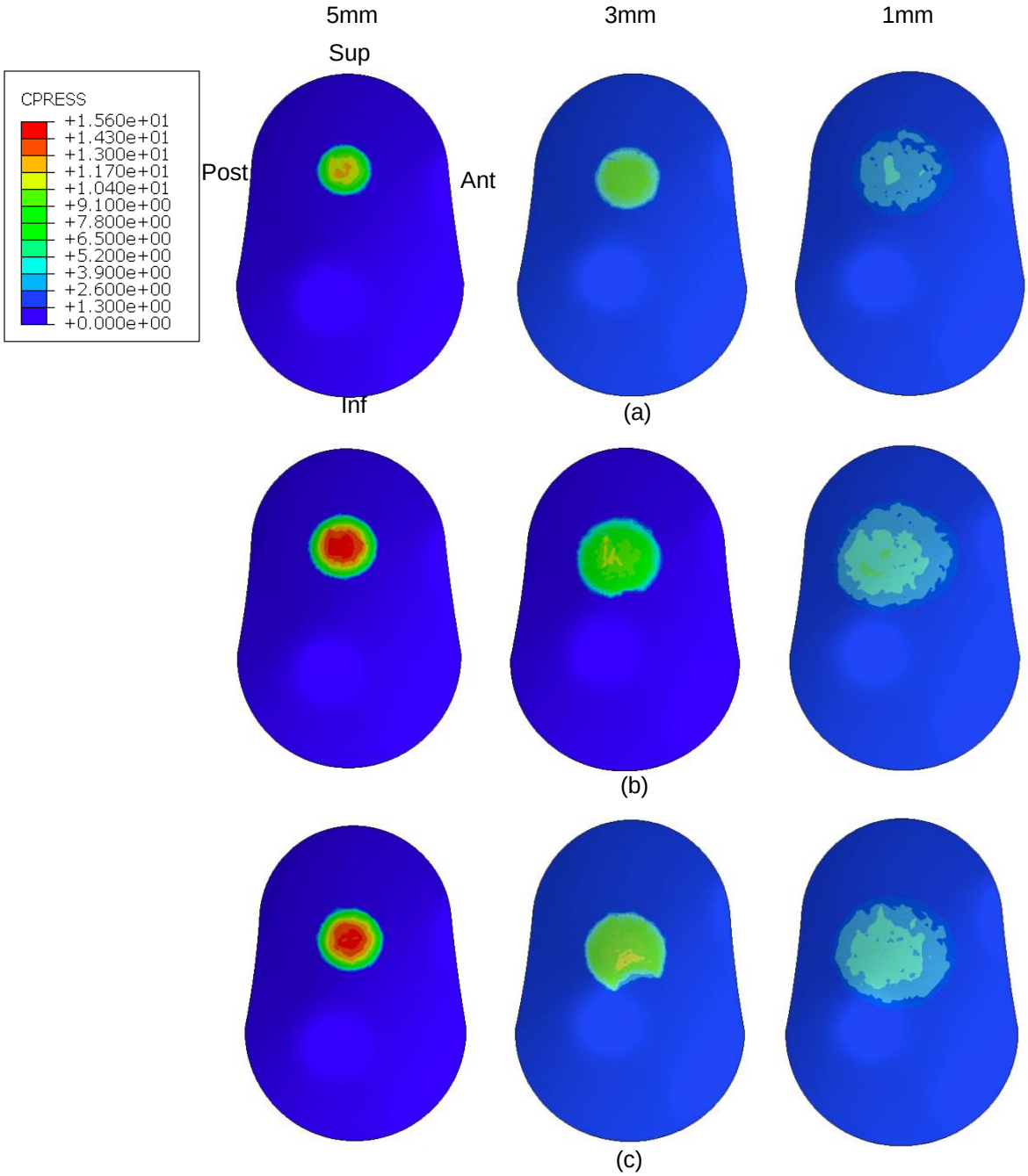

Figure A.0.1: Contact pressure for all GH configurations for (a) 30º of flexion, (a) 80º of flexion and (c) 105º of flexion. The color scale presented is applicable to all figures.